AIAA SciTech Forum
11–15 & 19–21 January 2021, VIRTUAL EVENT
AIAA Scitech 2021 Forum

10.2514/6.2021-1427

CFD Comparisons with Updated NASA Juncture Flow Data

C. L. Rumsey, N. N. Ahmad, J.-R. Carlson*,
M. A. Kegerise, D. H. Neuhart, J. A. Hannon, L. N. Jenkins, C.-S. Yao, P. Balakumar, S. Gildersleeve†,
S. M. Bartram‡
NASA Langley Research Center, Hampton, VA 23681
T. H. Pulliam §,
M. E. Olsen¶
NASA Ames Research Center, Moffett Field, CA 94035
P. R. Spalart‖
Boeing Commercial Airplanes, Seattle, WA 98124

The purpose of the NASA Juncture Flow experiment is to acquire high-quality flowfield details deep in the corner of a wing-body junction specifically for the purpose of CFD validation. A second phase of testing was recently completed, which includes both laser doppler velocimetry and particle image velocimetry measurements. This paper describes the recent experiment and its results. It also makes detailed comparisons between the experimental data and a new version of a widely-used CFD turbulence model for Reynolds-averaged Navier-Stokes, which was recently developed to improve separated corner flow predictions. The CFD results generally produce very good qualitative agreement with the experiment, although they are less accurate inside the separation region, as expected.

Nomenclature

C_2,C_3	constants in Spalart-Allmaras model
C'_{cr1},C'_{cr2}	constants used in QCR2020 model
C''_{cr1},C''_{cr2}	functions used in QCR2020 model
C_{fw1},C_{fw2}	constants used in QCR2020 model
c	crank chord = 557.174 mm
$c_{f,x}$	surface skin friction coefficient in the x direction
c_{r1},c_{r2},c_{r3}	constant in rotation-curvature correction model
c_{v1}	constant in Spalart-Allmaras model
c_{w2},c_{w3}	constants in Spalart-Allmaras model
D	function in rotation-curvature correction model
d	distance to the nearest wall, m
f_{v1},f_{f2}	variables in Spalart-Allmaras model
f_{r1}	function in rotation-curvature correction model
f_w	function in Spalart-Allmaras model
g	function in Spalart-Allmaras model
k	turbulent kinetic energy, m^2/s^2
M	Mach number
O_{ij}	tensor used in QCR2020 model
Re_c	Reynolds number based on crank chord

*Research Scientist, Computational AeroSciences Branch, Mail Stop 128.
†Aerospace Engineer, Flow Physics and Control Branch, Mail Stop 170.
‡Equipment Specialist, Advanced Measurement and Data Systems Branch, Mail Stop 493.
§Retired Senior Research Scientist.
¶Research Scientist, Aerothermodynamics Branch, Mail Stop N230-2.
‖Retired Boeing Senior Technical Fellow.

r	function in Spalart-Allmaras model
r^*	function in rotation-curvature correction model
$\hat{r}$	function in rotation-curvature correction model
S	strain magnitude term in rotation-curvature correction model, s^{-1}
S_{ij}	strain rate tensor, s^{-1}
$\overline{S}$	function in Spalart-Allmaras model, s^{-1}
$\hat{S}$	source term in Spalart-Allmaras model, s^{-1}
U	velocity, m/s
u_i	(u_1,u_2,u_3), Cartesian velocity components (u,v,w), m/s
u'_i	(u'_1,u'_2,u'_3), velocity fluctuation (u',v',w'), m/s
$u'_{i,s}$	($u'_{1,s}$,$u'_{2,s}$,$u'_{3,s}$), velocity fluctuation in the streamwise axis system (u'_s,v'_s,w'_s), m/s
$u'_i u'_j$	velocity fluctuation correlation tensor, m^2/s^2
W_{ij}	vorticity tensor, s^{-1}
x_i	(x_1,x_2,x_3), Cartesian coordinates (x,y,z), m (mm where noted)
α	angle of incidence, deg.
δ_{ij}	Kronecker delta
ϵ_{ijk}	Levi-Civita permutation tensor
κ	von Karman constant
μ_t	turbulent eddy viscosity, $kg/(ms)$
ν	molecular kinematic viscosity, m^2/s
$\hat{\nu}$	Spalart-Allmaras turbulence variable, m^2/s
ρ	density, kg/m^3
τ_{ij}	Reynolds stress tensor, $-\langle \rho u'_i u'_j \rangle$, $kg/(ms^2)$
χ	variable in Spalart-Allmaras model
Ω	vorticity, s^{-1}
Ω_s	modified vorticity, s^{-1}
Ω'_m	rotation term in rotation-curvature correction model, s^{-1}
ω	vorticity magnitude term in rotation-curvature correction model, s^{-1}
ω_{ij}	modified vorticity in rotation-curvature correction model, s^{-1}
$\langle\ \rangle$	long time average
Subscript	
$QCR2020$	QCR2020 model
ref	reference
Superscript	
L	linear model

I. Introduction

Predicting the location and extent of corner-flow separation has been challenging for CFD methods over the years (see, e.g., Vassberg et al. [1]). Accurate predictions of such flows are believed to have potential impact on the design and analysis of many aerodynamic flows of interest; for example, corner flow separation may play a role near maximum lift conditions [2]. An extensive experimental campaign was undertaken at NASA to help improve the understanding of aerodynamic flows in junction regions, and to provide high-quality flowfield data for use in CFD validation and CFD modeling improvement efforts. The NASA Juncture Flow (JF) experiment [3–6] was designed to be a "CFD validation" experiment of a wing-fuselage junction flow that experiences separation. This project involved an integrated CFD-experimental team, and significant resources and effort went into collecting data required for unambiguous CFD validation, such as extensive boundary conditions and uncertainty estimates.

The first set of JF tests [3], conducted in 2017-2018 in the NASA Langley Research Center 14- by 22-Foot Subsonic Tunnel (14x22), provided mean and turbulence flowfield data from laser doppler velocimetry (LDV) measurements taken through windows on the fuselage. A second JF entry was conducted in 2020. The new entry added flowfield results at another angle of attack, expanded the number of LDV locations, and acquired particle image velocimetry (PIV) data in the separated region. These new data are reported here, and are also available on the NASA Langley Turbulence Modeling Resource (TMR) website [7].

Several Reynolds-averaged Navier-Stokes (RANS) CFD efforts have been conducted to date, comparing JF pre-

dictions with the experiment [8–17]. These efforts, involving several different turbulence models, have included grid-resolution and grid-adaption studies (to ascertain the influence of numerical discretization errors on quantities of interest) as well as free-air versus in-tunnel studies (to ascertain the influence of wind tunnel walls). Other CFD efforts have included scale-resolving methods [18–22], which are inherently unsteady and designed to resolve the large turbulent eddies away from walls.

In the previous comparisons, RANS methods used in conjunction with a linear eddy viscosity model (via the Boussinesq constitutive relation) tended to dramatically overpredict the size of corner separation. This overprediction occurs because of the inability of linear models to capture differences between the normal stress components that lead to streamwise vorticity near corners [23]. This stress-induced vorticity delays the onset of corner separation. RANS with nonlinear constitutive relations fared far better, but were still not perfect regarding their prediction of flowfield quantities and separation size. For example, results with the Spalart-Allmaras (SA) model [24] with Rotation-Curvature (RC) correction [25] were significantly improved when used in conjunction with the Quadratic Constitutive Relation—QCR2000 [26] or QCR2013 [27]—but the length of the separation was still overpredicted by roughly 30%. Use of RANS with a particular full Reynolds Stress Model (RSM) [13] yielded better results, but a different RSM [14] dramatically underpredicted the separation size. It should be pointed out that in some of the above mentioned RANS studies, results using ostensibly the same turbulence model in different codes produced inconsistent results, for unknown reasons. However, we have high confidence in the SA-RC-QCR results obtained by the codes FUN3D [28] and OVERFLOW [29] because both codes have undergone extensive verification testing [7], and their results have also been consistent for this (and other) applications.

As a direct result of the experimental data and RANS comparisons to date, Rumsey et al. [30] developed QCR2020. This improved version of QCR was found to predict variations in the normal stresses better, and consequently improved results for the JF corner separation size.

The scale-resolving methods recently applied to the JF problem have fared reasonably well, although they are far more costly than RANS. Delayed detached-eddy simulations (DDES) yielded reasonable separation predictions [20, 22], but exhibited sensitivity to grid, probably associated with the shielding function. Wall-modeled large-eddy simulations (WMLES) tended to underpredict the size of separation on the grids used to date, and grid topology in the corner region could be influential [18, 19]. Lattice-Boltzmann (LB) results [21] were reasonable in terms of separation size, but the bubble shape was somewhat different than in the experiment. In all scale-resolving calculations, an effective tripping strategy was crucial.

In this paper, highlights of the experimental data from the 2020 test are described. Comparisons are made with RANS CFD results from two NASA CFD codes using the SA-RC model in conjunction with the latest QCR2020. In particular, comparisons are made with planar data taken in the corner region with both LDV and PIV. At the end, conclusions are drawn and future juncture-flow plans are outlined.

II. Phase 2 Wind Tunnel Test

A photograph of the JF test article is shown in Fig. 1. This full-span, sting-mounted, wing-body configuration has approximate length of 4.8 m and approximate width (wing tip to wing tip) of 3.4 m. The fuselage was specially designed to house movable laser systems, which could be used to measure flowfield details through windows on the fuselage port side.

A. Overview

The Phase 2 wind tunnel test conducted in early 2020 in the 14x22 used the same fuselage and truncated F6 wing from the second-half of the Phase 1 test. A leading-edge fillet, or "horn," was again included on the wing to mitigate the leading edge horseshoe vortex. With the F6-based wing, corner separation occurred in the wing-body junction at all angles of incidence tested in the range $-10^\circ < \alpha < 10^\circ$. Measured using oil flow, the size of the separation varied between about 70 and 150 mm in length and about 20 and 55 mm in width (for $-2.5^\circ < \alpha < 10^\circ$), and increased with increasing incidence angle. These separation sizes were felt to be optimal for testing, validating, and improving current turbulence model capabilities.

Specifically, the Phase 2 test objectives were:

1. Repeats of some lines of LDV data for verification and uncertainty quantification.
2. Fill in new data regions on the wing with LDV, including some "planes" (lines of data making a grid pattern).
3. Acquire LDV data at an additional angle of incidence of 7.5 deg.

4. Acquire flowfield velocity and Reynolds stress data with 3-component PIV in $x =$ constant planes over the wing trailing edge region at several angles of attack.
   (a) Include some locations and conditions also examined by LDV.
   (b) Provide a more complete picture of the JF flowfield in the juncture region.
5. Repeat test article pressure measurements and investigate specific regions identified from the Phase 1 test.
6. Repeat oil flow at several angles of incidence, including visualizations of both the wing and fuselage near the wing-fuselage junction.
7. Obtain tunnel wall pressure data.
8. Repeat tunnel wall rake boundary layer data on three walls.
9. Repeat laser scan of assembled test article, and Geographic Information System (GIS) scans of test article, mast, and sting positioning in the tunnel.
10. Document the transition behavior on the leading edge extension.

The nominal flow conditions were the same in all JF tests: $Re_c = 2.4 \times 10^6$, where c is the crank chord of $c = 557.174$ mm. The 14x22 is not a temperature controlled tunnel, so this resulted in a range of Mach numbers of roughly $0.175 < M < 0.205$, with a nominal value of $M = 0.189$ used by CFD. The boundary layers on the fuselage and wing upper and lower surfaces were tripped, and the trip effectiveness was verified using infrared thermography. The inboard-most portion of the wing (extending roughly 25 mm away from the fuselage near the wing leading edge) is located within the fuselage turbulent boundary layer. Further outboard, the boundary layer on the horn and wing leading edge is laminar up to the trip dots. The test article's wings and fuselage were instrumented for pressure, but no force or moment data were taken.

The current paper focuses on comparisons between CFD and experiment for some of the items listed above. A full accounting of all of the experimental data acquired can be found on the NASA TMR website [7]. One important change has been made regarding the method for computing uncertainties in the LDV data over the rear half of the wing. In the original data [3], the following uncertainty sources were accounted for: sampling variance for a given statistic, beam unit vector measurements, and Doppler frequency measurements. With additional data acquired in the Phase 2 test, other factors have been included following the method of Aeschliman and Oberkampf [31] and Rhode and Oberkampf [32]. With this method, uncertainty is estimated from a statistical analysis of residuals determined through comparison of measurements from certain pairings of runs and measurement points in space. The replicate runs at the same Reynolds number, test article attitude, test-section location, and flow-field location yields information about the random component of uncertainty. The replicate runs with the test article upright or inverted, but otherwise at the same Reynolds number, test article attitude, and flow-field location yields some information about the component of uncertainty due to flow nonuniformity and flow angularity, but also brings in uncertainty related to sting/mast blockage effects. In the end, the statistical analysis of residuals yields a 3 standard deviation (99.7% confidence interval) uncertainty estimate for each point in a flow-field survey.

Unfortunately, the laser system in the forward part of the fuselage failed during the Phase 2 test, so it was not possible to acquire repeat data (or new data) on the fuselage nose or near the wing leading edge. Therefore, the original uncertainty analysis from Kegerise and Neuhart [3] was not updated for the data taken on this region of the test article. In any case, the data taken during the Phase 1 test indicated a high degree of consistency in this region, even when inverting the test article in the tunnel.

B. Embedded LDV System Description

Some details regarding the LDV data are as follows. Laser doppler velocimetry (LDV) measurements were made with a pair of miniature fiber-optic based probes located inside the test article, and each one was mounted to a three-axis traverse system. The LDV probes provided measurements of three nonorthogonal instantaneous velocity components, and these were then used to calculate the three components of mean velocity, the six independent components of the Reynolds-stress tensor, and the ten independent components of the velocity triple products, all in the orthogonal body-fixed coordinate system. In addition, each probe had the capability to measure the particle position along the length of the measurement volume, and that feature could be used to achieve submeasurement-volume spatial resolution in that direction. Both probes were operated simultaneously and measurements were made only on the port side of the test

article. One probe was located near the trailing edge of the wing and was used to measure upstream of and inside the separated corner flow. The other probe was alternately used to measure the flow field in the leading-edge region of the wing and to measure the incoming boundary layer on the fuselage nose section.

For both probes, the measurement volume diameter and effective length was 140 μm and 180 μm, respectively. Seeding for the LDV measurements was provided by a smoke generator that produced a narrow distribution of particle sizes with a nominal diameter of 0.94 μm. Depending on where the measurement volume was located in the flow field, validated burst data rates of 100 to 500 bursts per second were achieved. In general, 15,000 to 30,000 samples were acquired at each point in the flow-field surveys, and those samples were then post processed to obtain the mean velocity components and turbulence statistics in a body-fixed coordinate system. Further details on the LDV system hardware, post processing, and uncertainty analysis can be found in Kegerise and Neuhart [3].

C. Embedded PIV System Description

The PIV data were being used in the JF experiment as a complementary technique to the LDV. Some of the PIV details are as follows. Building on the experience gained by applying PIV to the JF test article in prior tests [33], a stereo configuration was developed for the current test consisting of two high-speed cameras, light sheet optics, and a mirror that were mounted on a single translation stage inside the fuselage near the trailing edge of the wing. The translation stage enabled data to be acquired at different chordwise locations to capture the full expanse of the flow separation, from the initiation of separation upstream to the large, separated flow region near the trailing edge. The cameras featured a 2560 pixel by 1600 pixel sensor with a pixel size of 10μm by 10μm. In double exposure mode, the cameras were capable of acquiring full-frame images at a rate of 742 Hz. A 50 mm focal length lens was used with each of the cameras, which, at a working distance of 227.5 mm, provided a nominal field of view 119.4 mm wide and 89.7 mm high. A mirror was used in conjunction with the camera nearest to the front of the fuselage, so the two cameras could view the measurement area on opposite sides of the lightsheet.

The lightsheet was generated using an Nd-YLF high-speed laser with a maximum power of 40 milliJoules. Despite the generous amount of space inside the fuselage of the test article, there was not quite enough room to accommodate the cameras, translation system, and laser head. As such, the laser head was located below the test section and a fiber optic cable was used to transmit the laser light from the laser to the light sheet optics in the test article. The light sheet was projected over the wing in the spanwise direction, which helped to minimize potential issues with flare off the wing surface encountered in prior tests. This arrangement put the cameras in back-scatter relative to the direction of the projected laser light, but the particles were still exposed well due to the proximity of the cameras to the measurement area. One limitation created by projecting the light sheet from inside the model was the "blooming" that occurred at the location where the light sheet passed through the window. This "blooming" blocked the region close to the fuselage in the views of both cameras and as a result, the innermost edge of the measurement area ended up being 5 mm away from the fuselage ($y = -241.1$ mm). Despite this limitation, the PIV results provide sufficient overlap with LDV and CFD to enable detailed comparisons in regions of interest.

The seeding system and method used for the LDV measurements was also used for the PIV measurements. Particles were injected into the flow at specific intervals to seed the entire tunnel. This proved to be a very effective strategy for obtaining sufficient particle density in the wing-fuselage junction where the flow velocity can be significantly lower than the freestream.

In total, the PIV system was used to acquire over 1.3 million images at 65 different locations: 38 locations between $x = 2831.6$ mm and $x = 2962.6$ mm at $\alpha = 5^\circ$, 24 locations between $x = 2832.6$ mm and $x = 2953.2$ mm at $\alpha = 7.5^\circ$, and 3 locations between $x = 2899.6$ mm and $x = 2953.2$ mm at $\alpha = -2.5^\circ$. A minimum of 5000 images were acquired at each measurement location and processed using a multipass algorithm where an interrogation window of 64 pixels by 64 pixels and 75% overlap was used for the initial pass followed by 3 passes using an interrogation window of 32 pixels by 32 pixels and 75% overlap. The equivalent dimensions of the final interrogation window and the overlap correspond to a spatial resolution of 1.59 mm by 1.59 mm and a velocity vector spacing of 0.53 mm.

Figure 2 shows an example plot of PIV contours of u-velocity (larger view) along with LDV contours (superimposed) at $x = 2836.6$ mm, $\alpha = 7.5^\circ$. Note that the blank region in the PIV map was caused by one of the "ribs" in the fuselage window, which obscured the view. This figure exemplifies several things that apply to most of the flowfield contour figures to follow: (1) the PIV region extended over a greater region than the LDV; (2) the PIV plane generally got to within about 5 mm of the fuselage, whereas the LDV got to within 0.5 mm of the model surfaces; (3) the results from the two types of measurements were usually very close, but sometimes differences were seen that exceeded the stated uncertainty in the measurements. This series of PIV tests represents one of the first uses of a high-speed PIV system in the 14x22 wind tunnel to measure both velocities and moments; much of the effort was focused on developing the capability. In all of the results shown in this paper, the LDV is considered primary.

III. Numerical Methods

Two NASA-developed CFD codes, FUN3D and OVERFLOW, were used in this study. All computations were performed in "free air" (tunnel walls were not accounted for). Previous studies (e.g., Rumsey et al. [11]) have looked at the influence of tunnel walls on CFD results. Wall effects on most of the flowfield quantities of interest were relatively small. In other words, the ability or inability of a CFD method or model to predict separated corner flow on this JF configuration can be adequately demonstrated using a free-air computation. Different from previous JF studies using these two CFD codes, the current work set transition on the fuselage, $x = 336$ mm behind the nose. This was done in order to achieve a more accurate representation of the oncoming fuselage boundary layer thickness. However, it ended up making little or no difference in the predicted separation or other quantities of interest. Transition was not set at specific locations on the wings (they were run "fully turbulent").

The grids employed for the current paper were the same "fine" grids from the previous study [11]. The unstructured mixed-element fine grid contained about 161 million nodes (half span), and the overset structured fine grid contained about 173 million nodes (full span). In the above reference, as well as in Rumsey et al. [30], the effect of grid refinement for each code was documented. The fine grids used in this paper were previously shown to yield sufficiently accurate results for all quantities of interest.

A. FUN3D

The NASA FUN3D [34,35] solver is an unstructured three-dimensional, implicit, Navier-Stokes code that is nominally second-order spatially accurate. Roe's flux difference splitting [36] is used for the calculation of the inviscid terms for all the results in this paper (other flux construction methods are also available). The use of flux limiters are grid and flow dependent (none were used here). Other details regarding the code can be found in the extensive bibliography that is accessible at the FUN3D website [28]. A farfield Riemann invariant boundary condition was imposed on the outer boundary, no-slip solid wall boundary conditions were applied on the test article, and symmetry conditions were used on the x-z symmetry plane.

B. OVERFLOW

The NASA OVERFLOW [29] solver uses structured overset grids to simulate fluid flow. All of the OVERFLOW cases were run with OVERFLOW 2.2O. The 3^{rd}-order Roe upwind scheme [36] was used for the convective fluxes, and the implicit solve was done using the ARC3D Beam-Warming scalar pentadiagonal scheme and low-Mach preconditioning [29]. Similar to FUN3D, free-air computations employed a farfield Riemann invariant boundary condition imposed on the outer boundaries, and no-slip solid wall boundary conditions were applied on the test article. OVERFLOW simulations were performed for the full test article, i.e., no symmetry plane assumption.

C. Turbulence Model

The Spalart-Allmaras turbulence model [24] with Rotation-Curvature correction [25] and QCR2020 [30] (SA-RC-QCR2020) was employed for all runs in this study. This is a one-equation RANS turbulence model given by:

$$\frac{\partial \hat{\nu}}{\partial t} + u_j \frac{\partial \hat{\nu}}{\partial x_j} = c_{b1}(f_{r1} - f_{t2})\hat{S}\hat{\nu} - \left[c_{w1} f_w - \frac{c_{b1}}{\kappa^2} f_{t2}\right]\left(\frac{\hat{\nu}}{d}\right)^2 + \frac{1}{\sigma}\left[\frac{\partial}{\partial x_j}\left((\nu + \hat{\nu})\frac{\partial \hat{\nu}}{\partial x_j}\right) + c_{b2}\frac{\partial \hat{\nu}}{\partial x_i}\frac{\partial \hat{\nu}}{\partial x_i}\right] \quad (1)$$

where $\hat{\nu}$ is the SA turbulence variable, ν is the molecular kinematic viscosity, d is the distance to the nearest wall, and the turbulence eddy viscosity is computed from

$$\mu_t = \rho \hat{\nu} f_{v1} \quad (2)$$

and

$$f_{v1} = \frac{\chi^3}{\chi^3 + c_{v1}^3} \quad (3)$$

$$\chi = \frac{\hat{\nu}}{\nu} \quad (4)$$

$$\hat{S} = \Omega + \frac{\hat{\nu}}{\kappa^2 d^2} f_{v2} \tag{5}$$

$$f_{v2} = 1 - \frac{\chi}{1 + \chi f_{v1}} \tag{6}$$

$$f_w = g \left[\frac{1 + c_{w3}^6}{g^6 + c_{w3}^6} \right]^{1/6} \tag{7}$$

$$g = r + c_{w2}(r^6 - r) \tag{8}$$

$$r = \min \left[\frac{\hat{\nu}}{\hat{S} \kappa^2 d^2}, 10 \right] \tag{9}$$

$$f_{t2} = c_{t3} \exp\left(-c_{t4} \chi^2\right) \tag{10}$$

$$\Omega = \sqrt{2 W_{ij} W_{ij}} \tag{11}$$

$$W_{ij} = \frac{1}{2} \left(\frac{\partial u_i}{\partial x_j} - \frac{\partial u_j}{\partial x_i} \right) \tag{12}$$

and the coefficients are: $c_{b1} = 0.1355$, $\sigma = 2/3$, $c_{b2} = 0.622$, $\kappa = 0.41$, $c_{w1} = \frac{c_{b1}}{\kappa^2} + \frac{1 + c_{b2}}{\sigma}$, $c_{w2} = 0.3$, $c_{w3} = 2$, $c_{v1} = 7.1$, $c_{t3} = 1.2$, and $c_{t4} = 0.5$. At viscous solid walls, the boundary condition is $\hat{\nu} = 0$, and in the freestream $\hat{\nu} = 3$.

The RC correction [25] comes in solely through the f_{r1} term:

$$f_{r1} = (1 + c_{r1}) \frac{2 r^*}{1 + r^*} \left[1 - c_{r3} \tan^{-1}(c_{r2} \hat{r}) \right] - c_{r1} \tag{13}$$

where

$$r^* = S / \omega \tag{14}$$

$$\hat{r} = \frac{2 \omega_{ik} S_{jk}}{D^4} \left(\frac{D S_{ij}}{D t} + (\varepsilon_{imn} S_{jn} + \varepsilon_{jmn} S_{in}) \Omega'_m \right) \tag{15}$$

$$S_{ij} = \frac{1}{2} \left(\frac{\partial u_i}{\partial x_j} + \frac{\partial u_j}{\partial x_i} \right) \tag{16}$$

$$\omega_{ij} = \frac{1}{2} \left[\left(\frac{\partial u_i}{\partial x_j} - \frac{\partial u_j}{\partial x_i} \right) + 2 \varepsilon_{mji} \Omega'_m \right] \tag{17}$$

$$S^2 = 2 S_{ij} S_{ij} \tag{18}$$

$$\omega^2 = 2 \omega_{ij} \omega_{ij} \tag{19}$$

$$D^2 = \frac{1}{2} \left(S^2 + \omega^2 \right) \tag{20}$$

and Ω'_m is zero for all computations in this paper. The constants are $c_{r1} = 1.0$, $c_{r2} = 12$, and $c_{r3} = 1.0$. The Lagrangian (material) derivative is:

$$\frac{D S_{ij}}{D t} \equiv \frac{\partial S_{ij}}{\partial t} + u_k \frac{\partial S_{ij}}{\partial x_k} \tag{21}$$

with the time term ignored for all of the computations in this paper, because they are solved as steady state.

The QCR2020 methodology [30] was designed to provide improvements in the Reynolds normal stress behavior near walls, compared to earlier versions of QCR. The linear ("L") turbulent stresses from SA-RC are modified via

$$\tau_{ij,QCR2020} = \tau_{ij}^{L} - C_{cr1}'' \left[O_{ik}\tau_{jk}^{L} + O_{jk}\tau_{ik}^{L} \right] - C_{cr2}'' \mu_t \sqrt{2W_{mn}W_{mn}}\delta_{ij} \tag{22}$$

with:

$$O_{ik} = 2W_{ik} / \sqrt{\frac{\partial u_m}{\partial x_n}\frac{\partial u_m}{\partial x_n}} \tag{23}$$

$$C_{cr1}'' = C_{cr1}'(1 + C_{fw1}f_w), \tag{24}$$

$$C_{cr2}'' = C_{cr2}'(1 + C_{fw2}f_w), \tag{25}$$

and $C_{cr1}' = 0.20$, $C_{cr2}' = 2.15054$, $C_{fw1} = 2.0$, $C_{fw2} = 0.3$. A slight variant of the f_w function (Eq. (7)) is used in QCR2020. Instead of employing Eq. (5) in the definition of r that goes into g, the f_w variant uses:

$$\hat{S} = \begin{cases} \Omega_s + \bar{S} & \text{if } \bar{S} \geq -C_2\Omega_s \\ \Omega_s + \frac{\Omega_s(C_2^2\Omega_s + C_3\bar{S})}{(C_3 - 2C_2)\Omega_s - \bar{S}} & \text{if } \bar{S} < -C_2\Omega_s \end{cases} \tag{26}$$

$$\Omega_s = [0.5(2W_{ij}W_{ij} + 2S_{ij}S_{ij})]^{1/2} \tag{27}$$

$$\bar{S} = \frac{\hat{\nu}}{\kappa^2 d^2} f_{v2} \tag{28}$$

with $C_2 = 0.7$ and $C_3 = 0.9$. The f_w variant is intended to improve numerical robustness and iterative convergence behavior; it has little or no impact on the solution. Although not done here, the f_w variant could also be used in Eq. (1) with little perceptible impact.

As described in Rumsey et al. [30], QCR2020 produces a greater separation between the Reynolds normal stresses near the wall than earlier versions of QCR, in better agreement with experiment (JF and square duct flow) and DNS (flat plate boundary layer). In particular, for a system with x streamwise and y normal to the wall, $\langle u'u' \rangle$ and $\langle w'w' \rangle$ are both increased near the wall (the latter only slightly), whereas $\langle v'v' \rangle$ is generally decreased. It is the $C_{cr1}'' \left[O_{ik}\tau_{jk}^{L} + O_{jk}\tau_{ik}^{L} \right]$ term in eq. (22) that is responsible for this augmented separation between the normal stress components. On the other hand, the $C_{cr2}'' \mu_t \sqrt{2W_{mn}W_{mn}}\delta_{ij}$ term moves all normal stress curves equally, at a given height above the wall. In other words, the differences between the Reynolds normal stresses are controlled by the first term, while the general position of the group is controlled by the second term, as a function of wall distance. It should also be noted that, as described in Perkins [23], the $\langle u'u' \rangle$ Reynolds normal stress component has no influence on streamwise vorticity along a junction corner aligned with the x direction. So the near-wall behavior of the other components are likely to be more important in the juncture flows under consideration.

A minor turbulence model variant for SA-based models was employed by OVERFLOW. Termed "noft2", this variant sets $f_{t2} = 0$ in the base SA model. Functionally, for fully-turbulent solutions at sufficiently high Reynolds numbers, there is no difference resulting from this change [7]. Throughout the paper, the "noft2" designation has been dropped.

IV. Results

In this section, some comparisons are shown between the latest experimental data and RANS CFD results. Only a sampling of representative comparisons are shown. The full set of experimental data can be found at the NASA TMR website [7].

A. Test Article Pressures

Previous JF papers have shown comparisons of pressure coefficient on the test article at $\alpha = 5^\circ$ and -2.5° [9–11]. Here, only C_p comparisons at the new angle of incidence of $\alpha = 7.5^\circ$ are shown. However, it is important to note that the pressure data obtained in the 2020 test supersede the preliminary data from 2017-2018. In particular, on the wing, the peak C_p at the $y = -254$ mm station (which stood out as a location of concern from previous comparisons) is now different than previously shown. Also, uncertainty estimates are now included in the final reported pressures, representing two standard deviations from nine different runs (including three with the test article inverted in the tunnel) and both left and right wings.

Figures 3 and 4 show C_p comparisons at seven span stations on the wing. With the exception of inside the separation region (Fig. 3(b) inset) and at the wing tip ((Fig. 4(d)), the two CFD codes agree almost perfectly on their respective fine grids. Previously [11], it was shown that grid convergence was very difficult to achieve in these two areas. Nonetheless, differences on this grid level are relatively small. Agreement between CFD and experiment is generally excellent. Figure 5 shows selected C_p comparisons at five fuselage stations. For clarity, in Figs. 5(b) through (e), the abscissa is the angle θ measured from the center of the fuselage with $\theta = -90^\circ$ representing the bottom of the fuselage and $\theta = 90^\circ$ representing the top ($\theta = 0^\circ$ points out of the center side of the fuselage). Again, the two codes agree well with each other and with the experimental data.

B. Flowfield Velocities and Reynolds Stresses: Upstream Conditions on the Fuselage

Figure 6 shows CFD comparisons with LDV data for $\alpha = 5^\circ$ at a location on the fuselage nose, at the station $x = 1168.4$ mm. Other comparisons at this location at $\alpha = -2.5^\circ$ are not shown here, and no experimental data are available at this location for $\alpha = 7.5^\circ$. This location on the fuselage essentially represents a kind of "boundary condition" location very far upstream of the region of interest, where the flow is fully attached and CFD is expected to perform well. As seen in Fig. 6(b), the velocity components were captured very well by the CFD. Figure 6(c) shows that two of the turbulent normal stresses, $\langle v'v' \rangle$ and $\langle w'w' \rangle$, were also predicted reasonably well, but $\langle u'u' \rangle$ was underpredicted. This underprediction is typical of many RANS models. However, this comparison using QCR2020 represents a significant improvement over earlier predictions using QCR2000 or QCR2013. See Rumsey et al. [30]. For all velocity components and Reynolds stresses at this location, the two CFD codes FUN3D and OVERFLOW agree nearly perfectly.

Both $\langle u'v' \rangle$ and $\langle v'w' \rangle$, shown in Fig. 6(d), were predicted well by the CFD, but $\langle u'w' \rangle$ was off. This particular misprediction is a result of the fact that the CFD error in the streamwise normal stress "bleeds" over into the $\langle u'w' \rangle$ shear stress component expressed in the body-axis system. From Fig. 6(b), it can be deduced that the local flow direction at fuselage location $x = 1168.4$, $z = 0$ mm is tilted roughly 8.5° above the x-axis for the $\alpha = 5^\circ$ case. Using tensor rotations (see the appendix) for both CFD and experiment, the rotated Reynolds stresses were derived as shown in Fig. 6(e) and (f). Compare Fig. 6(e) with (c), and Fig. 6(f) with (d). There are only very small changes in the three normal stresses and in the principal shear $\langle u'_s v'_s \rangle$, but now the other (rotated) shear stresses go to near zero, and CFD agrees well with all of the shear stresses and two out of three of the normal stresses. Clearly, the error between CFD and experiment seen in $\langle u'w' \rangle$ in Fig. 6(d) came from the error in the CFD $\langle u'_s u'_s \rangle$, which affects the $\langle u'w' \rangle$ component expressed in the body-axis system.

It is worth noting that forcing the transition region on the fuselage nose helped to achieve a better prediction of boundary layer thickness at the $x = 1168.4$, $z = 0$ mm location. In earlier fully turbulent calculations, the CFD boundary layer was larger than shown here by a few mm.

C. Flowfield Velocities and Reynolds Stresses: In the Wing-Body Junction Region

In the Phase 2 experiment, LDV data were acquired in a tight "grid" pattern at several x-constant locations, making the reconstruction of 2-D contour maps possible. Planar PIV data were also acquired at some of the same locations, allowing for direct comparisons between PIV, LDV, and CFD. Figure 7 shows a downward view of the wing over the separated juncture region, showing the x-locations (also tabulated in Table 1) where the subsequent contours are plotted. This figure also shows the CFD streamlines from FUN3D for each angle of attack, which are indicative of the relative sizes of the computed separation regions (although not shown, OVERFLOW results were nearly the same). From oil flow, the apex of separation occurred near: $x = 2837$ mm for $\alpha = 7.5^\circ$, $x = 2851$ mm for $\alpha = 5^\circ$, and $x = 2893$ mm for $\alpha = -2.5^\circ$. These locations, along with the approximate separation bubble widths from the oil flow, are indicated with blue arrows. The SA-RC-QCR2020 RANS turbulence model does an excellent job capturing the variation of the separation region on this JF test article with angle of incidence.

Table 1. The x-locations (mm) where LDV and PIV data are plotted.

α, deg.	Method	Loc. 1	Loc. 2	Loc. 3	Loc. 4	Loc. 5	Loc. 6
7.5	LDV	2747.6	2790.6	2826.6	2836.6	2892.6	
	PIV				2836.6	2893.4	
5.0	LDV	2747.6	2789.6	2811.6	2852.6	2892.6	
	PIV				2852.6		
-2.5	LDV	2747.6	2815.6	2849.6	2887.6		2922.6
	PIV					2899.6	

1. Results at $\alpha = 7.5^\circ$

First, comparisons are shown for an incidence angle of $\alpha = 7.5^\circ$. Figures 8 through 10 show contour plots for the velocity components and Reynolds stresses at the location $x = 2747.6$ mm on the wing. These figures show LDV in the left hand column, with FUN3D center and OVERFLOW right. PIV was not measured this far forward. The viewpoint is looking forward in the juncture region over the port wing. The wing surface is indicated by the diagonal black line near the bottom of each figure, and the fuselage surface is represented by the vertical black line near the right of each figure. An outline is included in the CFD figures to show the extent of the LDV data collected. The LDV was typically measured to within 0.5 mm of the walls. Note that OVERFLOW used postprocessing interpolation to get its contours, so its solution is not shown all the way to the walls in the figures, even though it was computed.

One reason for focusing at this particular station is that it was the furthest forward location measured over the wing by the LDV Probe 2. The location shows the state of CFD relative to experimental data over the wing upper surface well upstream of where separation occurs. Unlike at the $x = 1168.4$ station far upstream on the fuselage, here some relatively small differences can be seen between FUN3D and OVERFLOW. As discussed in Rumsey et al. [11], CFD discretization errors grow more dominant as the separation region is approached.

In terms of velocity maps, Figs. 8(a)–(i) show that the two CFD codes were very close to each other, but not identical. They also differed to some degree from the experimental data. In particular, in Figs. 8(a)–(c), the u-component of velocity in the CFD shows higher momentum near the corner than in the experiment. This same behavior was seen previously [11,12,14,17] in line plots using a variety of different RANS models. The v-contours (Figs. 8(d)–(f)) show CFD with stronger spanwise flow (dark blue contours near the wing surface) outboard (to the left) of $y = -250$ mm, but reasonable agreement very near the corner. In fact, the red "hot spot" occurring near the corner of both experiment and CFD is indicative of the stress-induced streamwise vortex described in the Introduction, which is pushing flow toward the right at this location. The presence of this vortex helps to delay separation onset [11, 30]. Finally, the w-contours show reasonable agreement between CFD and experiment, with some small differences in the shape of the contours near $y = -240$ to -250 mm about 10 to 20 mm above the wing.

Reynolds normal stresses are shown in Fig. 9. The $\langle u'u' \rangle$ was underpredicted by the CFD along both walls (away from the corner), as expected. The $\langle v'v' \rangle$ was predicted generally well, but the $\langle w'w' \rangle$ was predicted to be too large in magnitude near the fuselage wall above the corner. The Reynolds shear stresses in Fig. 10 showed fair agreement overall between CFD and experiment, although the $\langle v'w' \rangle$ near the corner in the CFD was stronger than in the experiment.

To get a more quantitative picture, Fig. 11 shows extracted profiles in the same $x = 2747.4$ mm plane, along the line $y = -237.1$ mm. Here, the minor differences between the two CFD codes are evident, but they are much smaller than the differences between CFD and experiment. Figure 11(a) shows the usual overprediction in u-velocity near the corner by the CFD compared to the experimental data. In Figs. 11(c), the CFD slightly overpredicts $\langle v'v' \rangle$ and $\langle w'w' \rangle$ (although their relative differences are similar), and underpredicts $\langle u'u' \rangle$.

The turbulent shear stresses are generally well predicted by the CFD, except that $\langle u'w' \rangle$ is missed away from the wall. However, recall that errors in the streamwise component of turbulent normal stress can affect $\langle u'w' \rangle$ in the Cartesian frame when rotating in the x-z plane. By rotating the Reynolds stresses to the approximate streamwise axis system (Figs. 11(e) and (f)), the CFD shows better agreement with the $\langle u'_s w'_s \rangle$ component. Other Reynolds stress components show only minor effects of the rotation (which was taken to be -11° in the x-z plane). Note that determining the orientation of the streamwise axis system is not always straightforward. Here, the approximate angle of the wing surface was used, and any flow directionality out of the y-plane was ignored. In any case, we have

found that the effects of rotating the coordinate system on comparisons over this wing are not very large; i.e., general conclusions can still be made without it. Therefore, all remaining Reynolds stress profile comparisons are made only in the Cartesian frame.

In Fig. 12, the spatial evolution of several flowfield quantities are examined by looking at LDV and CFD results at identical stations, moving from the upstream station ($x = 2747.6$ mm) to about 56 mm beyond the start of separation. The flow direction is from top right to bottom left. Here, we focus on u (because it shows reverse flow), v (because it shows evidence of the stress-induced vortex), and $\langle u'w' \rangle$ (because this is the dominant Reynolds shear stress in the wing boundary layer whose streamwise direction is close to the x-axis and wall-normal direction is close to the z-axis). For the CFD, only FUN3D results are shown; OVERFLOW results were very similar. As seen in Figs. 12(a) and (b), nothing obvious changes in the u-contours until separation occurs somewhere near $x = 2837$ mm. The current SA-RC-QCR2020 model predicts this separation location well. Then, downstream at $x = 2892.6$ mm, there is a clear reversed flow region. The experiment and CFD appear to yield somewhat different shapes of this separated region.

Figures 12(c) and (d) indicate that the streamwise vorticity "hot spot" near the corner decreases slightly in strength as it moves downstream; this is reflected in the CFD. At the plane near the start of separation ($x = 2836.6$ mm) there is very good agreement between experiment and CFD in the spanwise flow near the wing outboard of the corner. Inside the separation, there is a double-lobed feature present in the experiment that is also captured to some degree by the CFD. In the $\langle u'w' \rangle$ contours (Fig. 12(e) and (f)), the CFD shows somewhat similar behavior as the experiment leading up to separation, but with less of a reduction in magnitude just above the corner bisector. Then, inside the separation region, both CFD and experiment show a strong Reynolds shear stress roughly aligned with the separated shear layer. However, the experimental shear levels are more pronounced in magnitude than the CFD.

Next, we examine contours at the plane near the start of separation ($x = 2836.6$ mm) in more detail, focusing on comparisons between LDV, PIV, and CFD. Figure 13 shows velocity contours. A black outline is included in the PIV and CFD maps to show the extent of the LDV measurements. Generally speaking, there is good agreement between the three methods, although (like at $x = 2747.6$ mm) the CFD indicates somewhat greater momentum near the corner. Note that the PIV did not measure close enough to the fuselage to be able to capture the "hot spot" in v-velocity seen in the LDV and CFD. Also, PIV appears to show a greater v-velocity very near the wing than LDV or CFD. CFD seems to miss the "reduction in downflow" that occurs somewhat along the corner bisector (evidenced in the w contours). However, the CFD shows similar contour bulges along the wing.

Figure 14 shows Reynolds normal stress contours. Again, there is fairly good agreement between both experimental methods and the CFD. The largest difference appears to be an overprediction of $\langle w'w' \rangle$ by the CFD above the corner. Finally, Fig. 15 shows Reynolds shear stress contours. Overall there is again fairly good agreement, although the PIV shows very high $\langle u'v' \rangle$ along its lower edge that is likely an artifact; this high positive shear is not present in the LDV or CFD.

For more quantitative comparisons, profiles were extracted from the planar $x = 2836.6$ mm data along a line at $y = -246.1$ mm. They are displayed in Fig. 16. In these plots, both FUN3D and OVERFLOW CFD results are included, and they demonstrate very consistent results with each other. As mentioned earlier, the CFD tends to overpredict the momentum in the juncture region. This is evident in the u profiles in Fig. 16(a). Also, the CFD shows more negative downflow (w) than in the experiment. Nonetheless, there is fairly good overall agreement in all of the turbulence quantities predicted by the CFD, and the PIV and LDV generally agree very well with each other (although the PIV does not always lie within the uncertainty bands of the LDV).

Figures 17 through 19 examine the flowfield in the plane at $x = 2892.6$ mm, post separation. However, note that the PIV location was slightly downstream of this (by 0.8 mm) at $x = 2893.4$ mm. Nonetheless, the PIV contours are included here for general comparison. LDV, PIV and CFD (FUN3D) indicate similar levels of reversed flow in the corner, and qualitative agreement with each other in terms of velocity contours (Fig. 17). RANS as usual shows more momentum (seen primarily in u contours) in the near-corner region, outside of the reverse-flow region. In the Reynolds normal stresses, the CFD indicates weaker $\langle u'u' \rangle$ and stronger $\langle v'v' \rangle$ and $\langle w'w' \rangle$ in the separated shear layer (Fig. 18). CFD mispredicts all of the Reynolds shear stresses (Fig. 19) in the same location. RANS is known to handle separated flows poorly [37], so it is no surprise that it is not doing as well in this region as it did in the attached flow region leading up to separation.

In Fig. 20, line plots extracted along $y = -246.1$ mm are shown. PIV and LDV show generally very good agreement with each other. The RANS results are notably different from the experimental data, although there are many qualitative similarities. Note also that at this station passing through the separated zone, the two CFD codes generally show reduced agreement with each other (likely due to greater discretization error).

2. Results at $\alpha = 5^\circ$

For $\alpha = 5^\circ$, trends are very similar to the earlier results at $\alpha = 7.5^\circ$. However, separation occurs slightly further downstream, near $x = 2851$ mm. For brevity, detailed results are not plotted at the upstream $x = 2747.6$ mm station. However, Fig. 21 shows the progression of a few flowfield contour levels of interest for LDV and CFD (FUN3D). Comparing this figure to Fig. 12, the results are seen to be very similar in appearance (although note that the planar locations are not all the same). Both CFD and experiment again indicate the presence of a streamwise vortex deep in the corner, and CFD again predicts the onset of separation reasonably well. Also, CFD still underpredicts the magnitude of the $\langle u'w' \rangle$ levels in the separated shear layer at the $x = 2892.6$ mm station.

Detailed comparisons between LDV, PIV, and CFD (FUN3D) are shown in Figs. 22 through 24. Comparing these plots to the $\alpha = 7.5^\circ$ case in Figs. 13 through 15, it is clear that the flowfields near the onset of separation for both cases are very similar. There is again fairly good agreement between both experimental methods and the CFD. Detailed line plots in Fig. 25 along $y = -246.1$ mm confirm this. Comparing Fig. 25 with Fig. 16, similar trends and agreement are evident.

3. Results at $\alpha = -2.5^\circ$

For $\alpha = -2.5^\circ$, only the flowfield progression of u, v, and $\langle u'w' \rangle$ are shown (Fig. 26). In this figure, LDV planar data are shown in the left plots along with one PIV plane at $x = 2899.6$ mm. Although at this angle of attack the separation is substantially delayed, to near $x = 2893$ mm, the general flowfield behavior leading up to separation is similar to the other angles of incidence. The SA-RC-QCR2020 RANS turbulence model again predicts the general behavior, including separation onset location, very well. In this figure, the flow at $x = 2922.6$ mm is not very far into the separated region, so the reversed flow area is smaller and the separated shear layer is not as evident in the $\langle u'w' \rangle$ contours as it was in Figs. 12 and 21.

V. Conclusions and Future Plans

Phase 2 of the NASA JF experiment was successfully conducted in early 2020. All of the test objectives were met, with the exception of acquiring repeated LDV data upstream on the test article nose and near the wing leading edge. The additional LDV data that were obtained over the wing yielded: (1) results at a new angle of incidence, (2) results at more locations over the wing, (3) data in planar fields over the wing, allowing for the construction of contour maps, and (4) a more comprehensive uncertainty analysis. PIV capability in the 14x22 wind tunnel was expanded, and planar data were acquired in the separated region, allowing comparisons to be made between the two measurement techniques (PIV and LDV) for both mean flow quantities and Reynolds stresses. Generally very good agreement between the two methods was seen, even deep in the separated region, although the PIV results did not always lie within the uncertainty bands of the LDV. The uncertainty in the PIV measurements (which has not yet been quantified) in principal should be large enough to cover the differences. A significant fraction of the PIV data is still being reduced. It contains a wealth of additional unsteady information not yet explored. Test article pressures, oil flow, and other documentation from the wind tunnel experiment expanded the understanding of the JF flowfield and improved the quality and usefulness of the JF data.

In a broad sense, the LDV and PIV methodologies for measuring the flowfield details were complementary. The LDV was able to measure closer to the walls on this configuration, and with greater accuracy than PIV, but was relatively slow to acquire because it measured only one point at a time. The PIV could attain much larger planar areas very rapidly. In terms of cost of hardware and setup time, the two methods were comparable.

A modification to a quadratic constitutive relation, termed QCR2020, was recently devised based on the NASA JF data. Here, it was used in conjunction with the SA-RC RANS model in two CFD codes. Results from the two codes were consistent, although discretization errors tended to be larger in and near the separation region. Nonetheless, the differences between the CFD codes were typically far smaller than differences between CFD and experiment, and a previous paper had examined grid sensitivity and found the "fine" grids used in this paper to be sufficient for the purpose of evaluating corner separation and flowfield details. Furthermore, previous CFD studies that included wind tunnel walls had shown that the ability of CFD to predict separated corner flow on this JF configuration can be adequately demonstrated using free-air computations, because the effect of the tunnel walls is relatively minor on the corner-flow quantities of interest. Although far from perfect, QCR2020 significantly improves the prediction of the turbulent normal stresses, allowing for very accurate predictions of the size of the JF separation region over a range of angles of incidence. Comparisons between CFD and both the LDV and PIV experimental techniques indicated generally very good qualitative agreement in velocities and Reynolds stresses, with CFD often (but not

always) producing similar contour shapes and levels as those measured by the LDV and PIV. The RANS tended to overpredict the momentum in the corner leading up to separation, and larger differences in general between CFD and experiment were noted downstream of separation.

A phase 3 experimental campaign is planned for JF in 2021 or 2022. This 14x22 wind tunnel entry will focus on providing LDV measurements over a different wing that yields both fully attached and incipient corner flow separation as a function of angle of incidence. This new set of data is expected to further challenge CFD methods, whose goal is the accurate prediction of the onset and progression of separation.

Appendix

The purpose of this appendix is to describe a typical Reynolds stress transformation. In general, for the NASA JF configuration, it is easy to draw conclusions *without* this transformation, but it is important for the reader to be aware of its impact. In all of the JF experimental measurements, the components of velocity and Reynolds stresses were measured in the body axis system (x along the centerline of the fuselage, y out the starboard wing, and z up). However, RANS turbulence models are primarily calibrated to obtain the turbulent shear stress aligned with the flow direction. Typically, RANS methods do not capture the Reynolds normal stresses well. The QCR2020 relation was devised in order to improve the ability of RANS to capture these normal components, but there are still errors. These errors in the normal components can affect the shear components when expressed in a different reference frame.

For brevity, only a 2-D rotation of the Reynolds stress tensor in the x-z plane is shown below. A 3-D generalization of the transformation is possible. The following transformation takes the Reynolds stresses in the Cartesian coordinate system to the coordinate system (subscript "s") that is rotated θ degrees in the x-z plane:

$$\begin{bmatrix} \langle u_s' u_s' \rangle & \langle u_s' v_s' \rangle & \langle u_s' w_s' \rangle \\ \langle u_s' v_s' \rangle & \langle v_s' v_s' \rangle & \langle v_s' w_s' \rangle \\ \langle u_s' w_s' \rangle & \langle v_s' w_s' \rangle & \langle w_s' w_s' \rangle \end{bmatrix} = \begin{bmatrix} \cos\theta & 0 & \sin\theta \\ 0 & 1 & 0 \\ -\sin\theta & 0 & \cos\theta \end{bmatrix} \begin{bmatrix} \langle u'u' \rangle & \langle u'v' \rangle & \langle u'w' \rangle \\ \langle u'v' \rangle & \langle v'v' \rangle & \langle v'w' \rangle \\ \langle u'w' \rangle & \langle v'w' \rangle & \langle w'w' \rangle \end{bmatrix} \begin{bmatrix} \cos\theta & 0 & -\sin\theta \\ 0 & 1 & 0 \\ \sin\theta & 0 & \cos\theta \end{bmatrix}. \quad (29)$$

This results in:

$$\langle u_s' u_s' \rangle = \langle u'u' \rangle \cos^2\theta + \langle w'w' \rangle \sin^2\theta + \langle u'w' \rangle \sin(2\theta) \quad (30)$$

$$\langle v_s' v_s' \rangle = \langle v'v' \rangle \quad (31)$$

$$\langle w_s' w_s' \rangle = \langle u'u' \rangle \sin^2\theta + \langle w'w' \rangle \cos^2\theta - \langle u'w' \rangle \sin(2\theta) \quad (32)$$

$$\langle u_s' v_s' \rangle = \langle u'v' \rangle \cos\theta + \langle v'w' \rangle \sin\theta \quad (33)$$

$$\langle u_s' w_s' \rangle = \frac{1}{2}(\langle w'w' \rangle - \langle u'u' \rangle) \sin(2\theta) + \langle u'w' \rangle \cos(2\theta) \quad (34)$$

$$\langle v_s' w_s' \rangle = -\langle u'v' \rangle \sin\theta + \langle v'w' \rangle \cos\theta. \quad (35)$$

Sample results using this transformation were shown in Figs. 6(e) and (f), and in Figs. 11(e) and (f).

Acknowledgments

This work was supported by the NASA Transformational Tools and Technologies (TTT) project of the Transformative Aeronautics Concepts Program.

References

[1]Vassberg, J. C., Tinoco, E. N., Mani, M., Rider, B., Zickuhr, T., Levy, D. W., Brodersen, O. P., Eisfeld, B., Crippa, S., Wahls, R. A., Morrison, J. H., Mavriplis, D. J., and Murayama, M., "Summary of the Fourth AIAA Computational Fluid Dynamics Drag Prediction Workshop," *Journal of Aircraft*, Vol. 51, No. 4, July-August 2014, pp. 1070–1089, doi: https://doi.org/10.2514/1.C032418.

[2]Rumsey, C. L., Slotnick, J. P., and Sclafani, A. J., "Overview and Summary of the Third AIAA High Lift Prediction Workshop," *Journal of Aircraft*, Vol. 56, No. 2, March-April 2019, pp. 621–644, doi: https://doi.org/10.2514/1.C034940.

[3]Kegerise, M. A. and Neuhart, D. H., "An Experimental Investigation of a Wing-Fuselage Junction Model in the NASA Langley 14- by 22-Foot Subsonic Tunnel," NASA/TM-2019-220286, June 2019, https://ntrs.nasa.gov/archive/nasa/casi.ntrs.nasa.gov/20190027403.pdf.

[4]Kegerise, M. A., Neuhart, D. H., Hannon, J. A., and Rumsey, C. L., "An Experimental Investigation of a Wing-Fuselage Junction Model in the NASA Langley 14- by 22-Foot Subsonic Wind Tunnel," AIAA Paper 2019-0077, January 2019, doi: https://doi.org/10.2514/6.2019-0077.

[5]Rumsey, C. L., Neuhart, D. H., and Kegerise, M. A., "The NASA Juncture Flow Experiment: Goals, Progress, and Preliminary Testing," AIAA Paper 2016–1557, January, 2016, doi: https://doi.org/10.2514/6.2016-1557.

[6]Rumsey, C. L., "The NASA Juncture Flow Test as a Model for Effective CFD/Experimental Collaboration," AIAA Paper 2018-3319, June 2018, doi: https://doi.org/10.2514/6.2018-3319.

[7]Rumsey, C. L., "NASA Langley Turbulence Modeling Resource Website," https://turbmodels.larc.nasa.gov, Accessed: 2020-10-21.

[8]Rumsey, C. L., Carlson, J.-R., Hannon, J. A., Jenkins, L. N., Bartram, S. M., Pulliam, T. H., and Lee, H. C., "Boundary Condition Study for the Juncture Flow Experiment in the NASA Langley 14x22-Foot Subsonic Wind Tunnel," AIAA Paper 2017-4126, June 2017, doi: https://doi.org/10.2514/6.2017-4126.

[9]Rumsey, C. L., Carlson, J.-R., and Ahmad, N. N., "FUN3D Juncture Flow Computations Compared with Experimental Data," AIAA Paper 2019-0079, January 2019, doi: https://doi.org/10.2514/6.2019-0079.

[10]Lee, H. C. and Pulliam, T. H., "OVERFLOW Juncture Flow Computations Compared with Experimental Data," AIAA Paper 2019-0080, January 2019, doi: https://doi.org/10.2514/6.2019-0080.

[11]Rumsey, C. L., Lee, H. C., and Pulliam, T. H., "Reynolds-Averaged Navier-Stokes Computations of the NASA Juncture Flow Model Using FUN3D and OVERFLOW," AIAA Paper 2020-1304, January 2020, doi: https://doi.org/10.2514/6.2020-1304.

[12]Abdol-Hamid, K. S., Ahmad, N. N., Carlson, J.-R., and Biedron, R. T., "Juncture Flow Computations using kL-Based Turbulence Models," AIAA Paper 2020-1305, January 2020, doi: https://doi.org/10.2514/6.2020-1305.

[13]Eisfeld, B., Togiti, V., Braun, S., and Sturmer, A., "Reynolds-Stress Model Computations of the NASA Juncture Flow Experiment," AIAA Paper 2020-1306, January 2020, doi: https://doi.org/10.2514/6.2020-1306.

[14]Zastawny, M. and Lardeau, S., "Application of Simcenter STAR-CCM+ for Assessment of the Impact of CFD Modelling Approach in NASA Juncture Flow Simulations," AIAA Paper 2020-2736, June 2020, doi: https://doi.org/10.2514/6.2020-2736.

[15]Aliaga, C. N., Chen, J., Selvanayagam, J., Ozcer, I. A., and Stokes, J., "Automatic Mesh Optimization for Wing-Fuselage Juncture Flow Separation Predictions," AIAA Paper 2020-2750, June 2020, doi: https://doi.org/10.2514/6.2020-2750.

[16]Wood, S. L., Anderson, W. K., Park, M. A., Balan, A., Karman, S., and Jacobson, K. E., "Reynolds-Averaged Navier-Stokes Computations of the NASA Juncture Flow Model Using Expert-Crafted and Adapted Grids," AIAA Paper 2020-2751, June 2020, doi: https://doi.org/10.2514/6.2020-2751.

[17]Abe, H., Mizobuchi, Y., and Matsuo, Y., "Effect of a Quadratic Constitutive Relation on Juncture Flow Computations," AIAA Paper 2020-2752, June 2020, doi: https://doi.org/10.2514/6.2020-2752.

[18]Iyer, P. S. and Malik, M. R., "Wall-modeled LES of the NASA Juncture Flow Experiment," AIAA Paper 2020-1307, January 2020, doi: https://doi.org/10.2514/6.2020-1307.

[19]Lozano-Duran, A., Moin, P., and Bose, S. T., "Prediction of Trailing Edge Separation on the NASA Juncture Flow Using Wall-Modeled LES," AIAA Paper 2020-1776, January 2020, doi: https://doi.org/10.2514/6.2020-1776 and https://doi.org/10.2514/6.2020-1776.c1.

[20]Balin, R., Wright, J., Patterson, J., Farnsworth, J. A., Evans, J. A., Lakhani, R., Spalart, P., and Jansen, K. E., "Hybrid Turbulence Model Computations of the NASA Juncture Flow Model Using PHASTA," AIAA Paper 2020-1777, January 2020, doi: https://doi.org/10.2514/6.2020-1777.

[21]Duda, B. M. and Laskowski, G. M., "Lattice-Boltzmann Very Large Eddy Simulations of the NASA Juncture Flow Model," AIAA Paper 2020-1778, January 2020, doi: https://doi.org/10.2514/6.2020-1778.

[22]Ghate, A. S., Housman, J. A., Stich, G.-D., Kenway, G. K., and Kiris, C. C., "Scale Resolving Simulations of the NASA Juncture Flow Model Using the LAVA Solver," AIAA Paper 2020-2735, June 2020, doi: https://doi.org/10.2514/6.2020-2735

[23]Perkins, H. J., "The Formation of Streamwise Vorticity in Turbulent Flow," *Journal of Fluid Mechanics*, Vol. 44, Part 4, 1970, pp. 721–740, doi: https://doi.org/10.1017/S0022112070002112.

[24]Spalart, P. R. and Allmaras, S. R., "A One-Equation Turbulence Model for Aerodynamic Flows," *Recherche Aerospatiale*, Vol. 1, 1994, pp. 5–21.

[25]Shur, M. L., Strelets, M. K., Travin, A. K., and Spalart, P. R., "Turbulence Modeling in Rotating and Curved Channels: Assessing the Spalart-Shur Correction," *AIAA Journal*, Vol. 38, No. 5, 2000, pp. 784–792, doi: https://doi.org/10.2514/2.1058.

[26]Spalart, P. R., "Strategies for Turbulence Modelling and Simulation," *International Journal of Heat and Fluid Flow*, Vol. 21, 2000, pp. 252–263, doi: https://doi.org/10.1016/S0142-727X(00)00007-2.

[27]Mani, M., Babcock, D. A., Winkler, C. M., and Spalart, P. R., "Predictions of a Supersonic Turbulent Flow in a Square Duct," AIAA Paper 2013-0860, January 2013, doi: https://doi.org/10.2514/6.2013-0860.

[28]"FUN3D Users Manual," https://fun3d.larc.nasa.gov, Accessed: 2020-10-21.

[29]Nichols, R. H. and Buning, P. G., "Users Manual for Overflow 2.2," https://overflow.larc.nasa.gov/home/users-manual-for-overflow-2-2, Accessed: 2020-10-21.

[30]Rumsey. C. L., Carlson, J.-R., Pulliam, T. H., and Spalart, P. R., Improvements to the Quadratic Constitutive Relation Based on NASA Juncture Flow Data," *AIAA Journal*, Vol. 58, No. 10, 2020, pp. 4374-4384, doi: https://doi.org/10.2514/1.J059683.

[31]Aeschliman, D. P. and Oberkampf, W. L., "Experimental Methodology for Computational Fluid Dynamics Code Validation," *AIAA Journal*, Vol. 36, No. 5, 1998, pp. 733–741, doi: https://doi.org/10.2514/2.461.

[32]Rhode, M. N. and Oberkampf, W. L., "Estimation of Uncertainties for a Model Validation Experiment in a Wind Tunnel," *Journal of Spacecraft and Rockets*, Vol. 54, No. 1, 2017, pp. 155–168, doi: https://doi.org/10.2514/1.A33563.

[33]Jenkins, L. N., Yao, C. S., and Bartram, S. M., "Flow-Field Measurements in a Wing-Fuselage Junction Using an Embedded Particle Image Velocimetry System," AIAA Paper 2019-0078, January 2019, doi: https://doi.org/10.2514/6.2019-0078.

[34]Anderson, W. and Bonhaus, D., "An Implicit Upwind Algorithm for Computing Turbulent Flows on Unstructured Grids," *Computers and Fluids*, Vol. 23, No. 1, 1994, pp. 1–22, doi: https://doi.org/10.1016/0045-7930(94)90023-X.

[35]Anderson, W., Rausch, R., and Bonhaus, D. L., "Implicit/Multigrid Algorithms for Incompressible Turbulent Flows on Unstructured Grids," *Journal of Computational Physics*, Vol. 128, 1996, pp. 391–408, doi: https://doi.org/10.1006/jcph.1996.0219.

[36]Roe, P. L., "Approximate Riemann Solvers, Parameter Vectors, and Difference Schemes," *Journal of Computational Physics*, Vol. 43, 1981, pp. 357–372, doi: https://doi.org/10.1016/0021-9991(81)90128-5.

[37]Uzun, A. and Malik, M. R., "Large-Eddy Simulation of Flow over a Wall-Mounted Hump with Separation and Reattachment," *AIAA Journal*, Vol. 56, No. 2, 2018, pp. 715–730, doi: https://doi.org/10.2514/1.J056397.

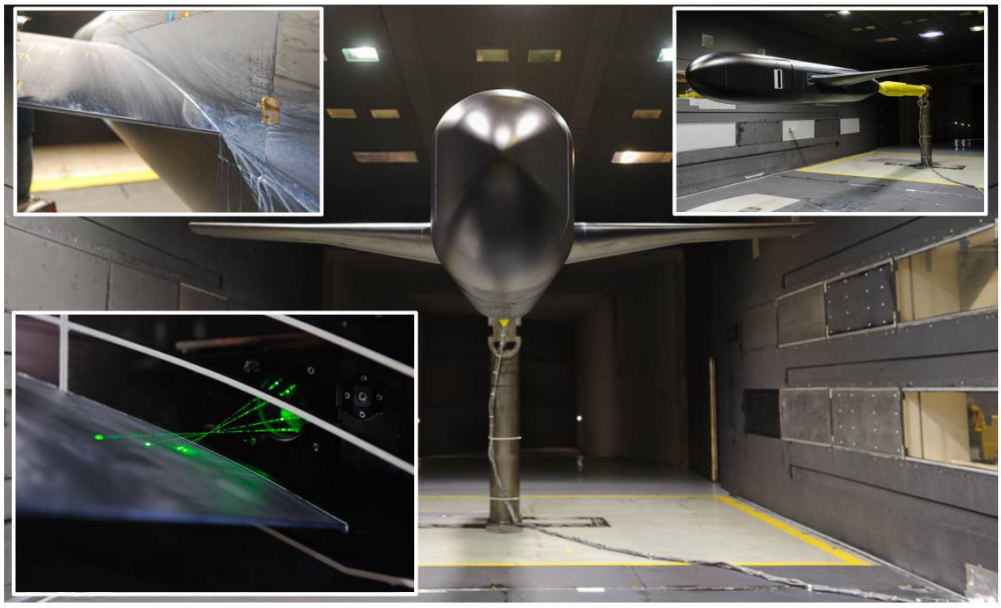

Figure 1. NASA Juncture Flow test article in the 14x22 wind tunnel.

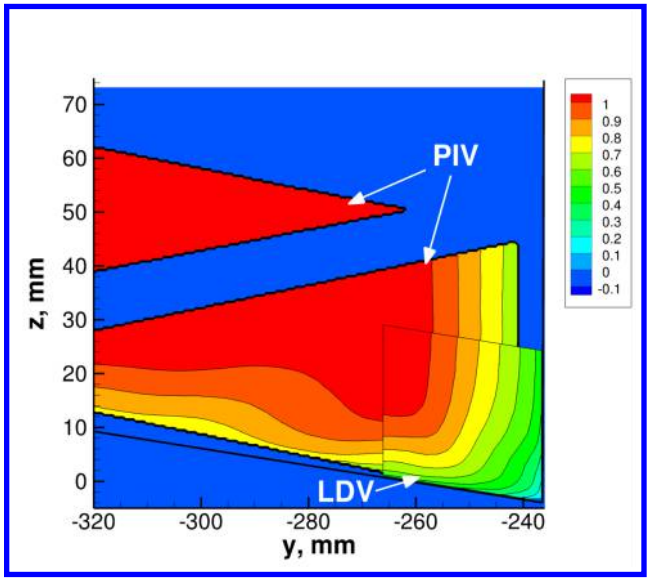

Figure 2. Example of PIV and LDV u/U_{ref} velocity contours at $x = 2836.6$ mm, $\alpha = 7.5°$.

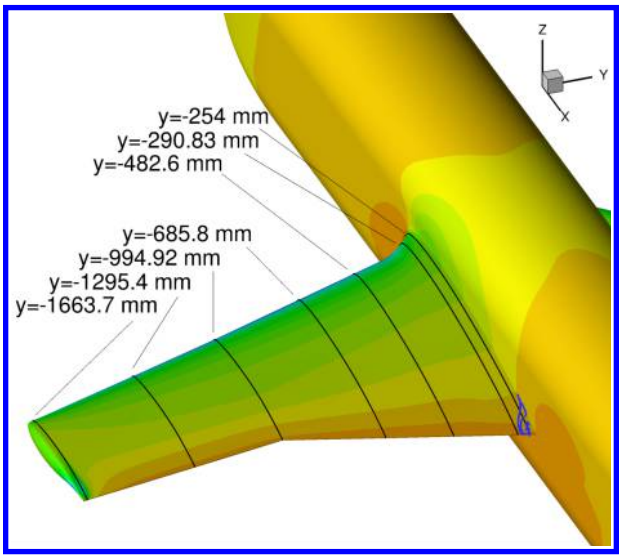

(a) Location of pressure taps (approximate size of computed separation at $\alpha = 7.5°$ also indicated)

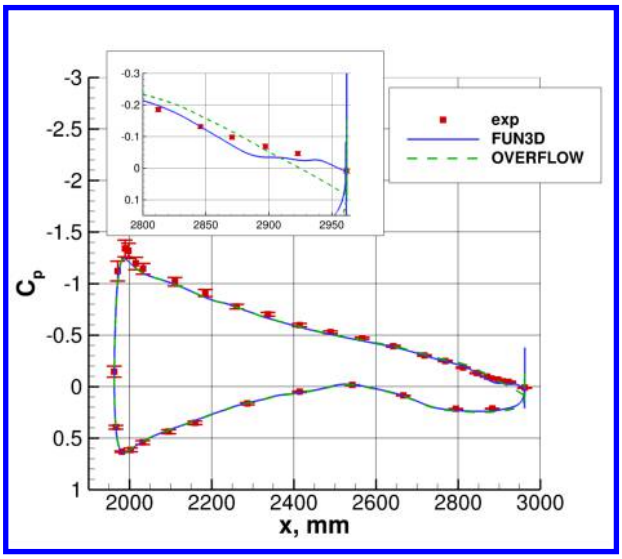

(b) $y = -254$ mm

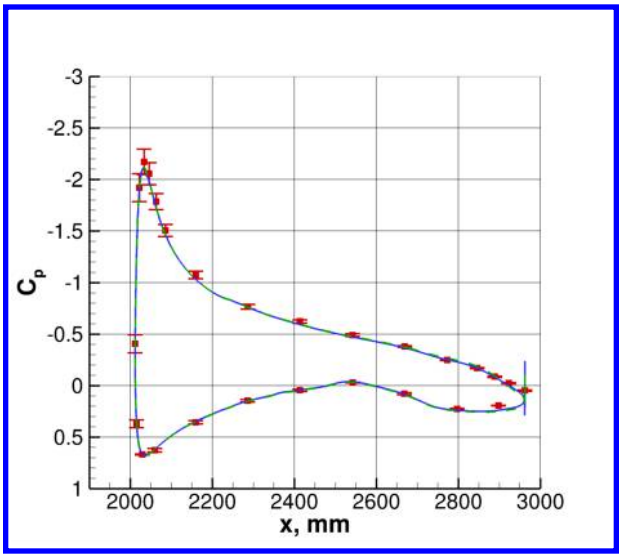

(c) $y = -290.83$ mm

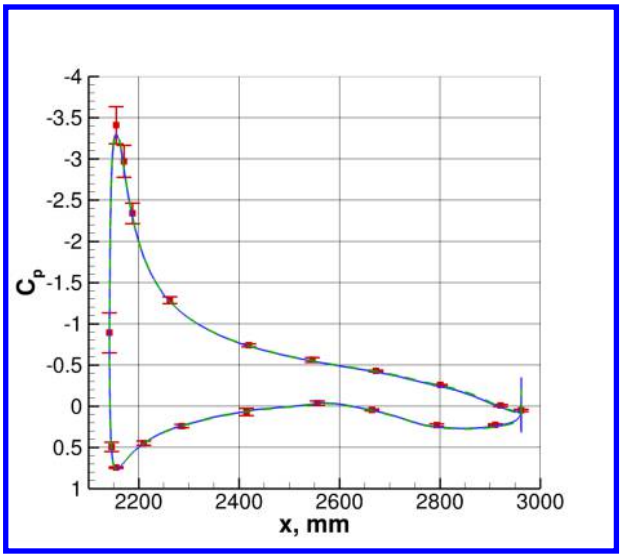

(d) $y = -482.6$ mm

Figure 3. Surface pressure coefficients on inner part of wing, $\alpha = 7.5°$.

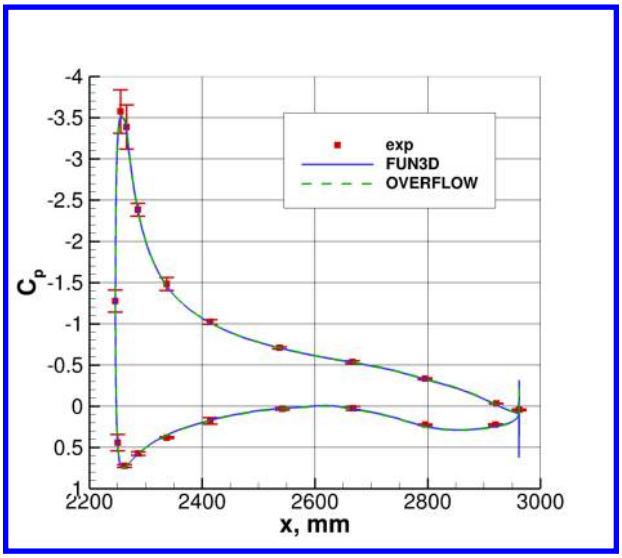

(a) $y = -685.8$ mm

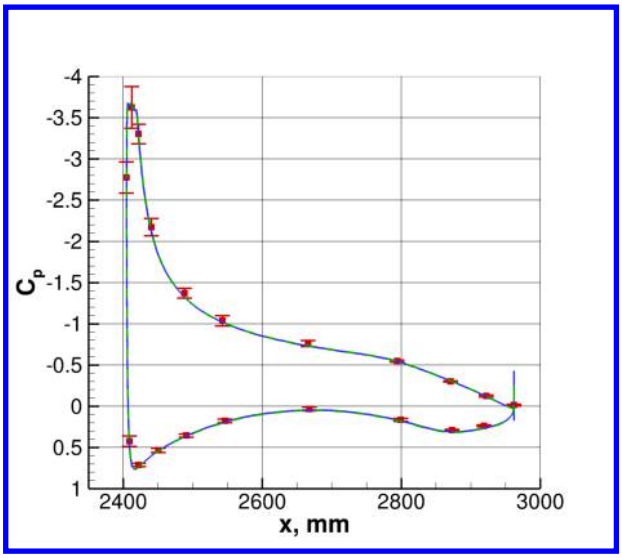

(b) $y = -994.92$ mm

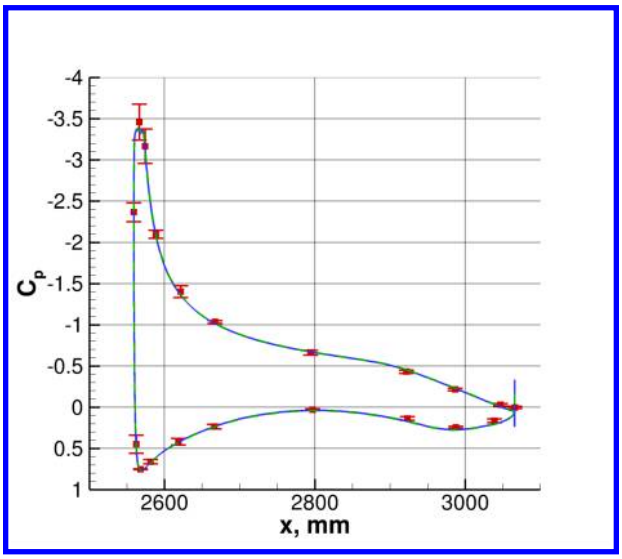

(c) $y = -1295.4$ mm

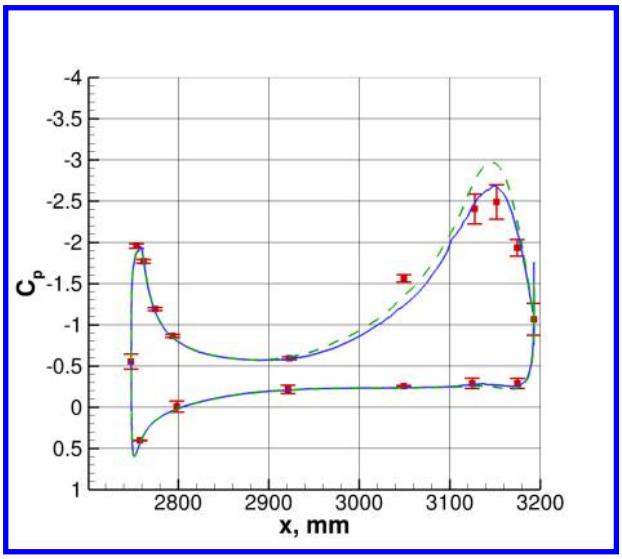

(d) $y = -1663.7$ mm

Figure 4. Surface pressure coefficients on outer part of wing, $\alpha = 7.5°$, see Fig. 3.

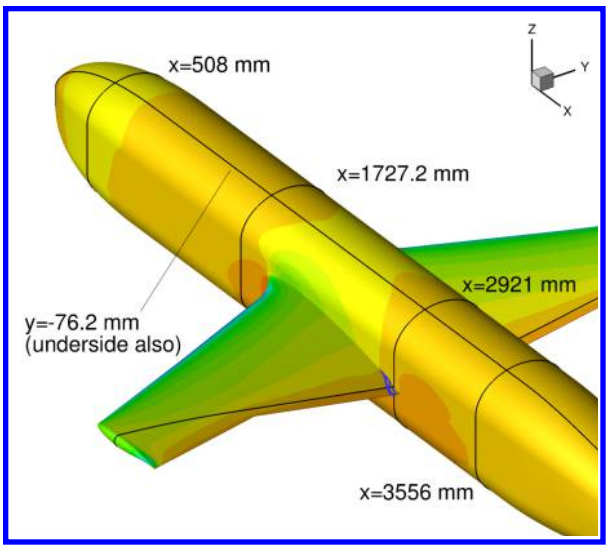

(a) Location of pressure taps (approximate size of computed separation at $\alpha = 7.5°$ also indicated)

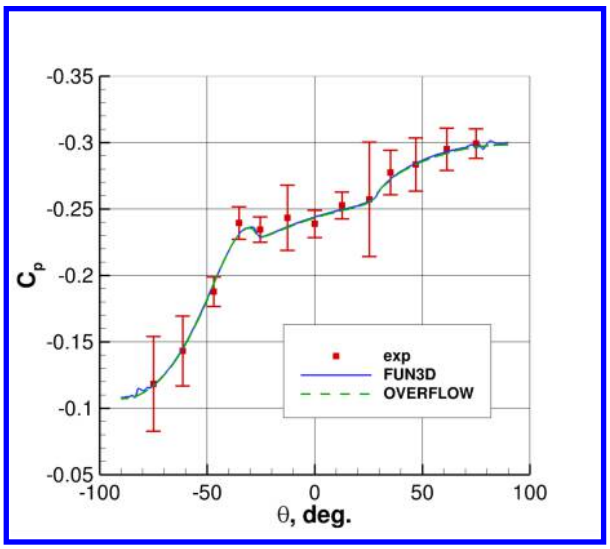

(b) $x = 508$ mm

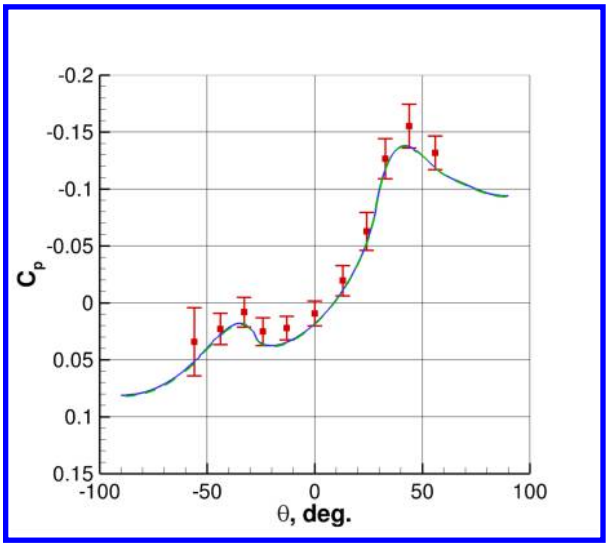

(c) $x = 1727.2$ mm

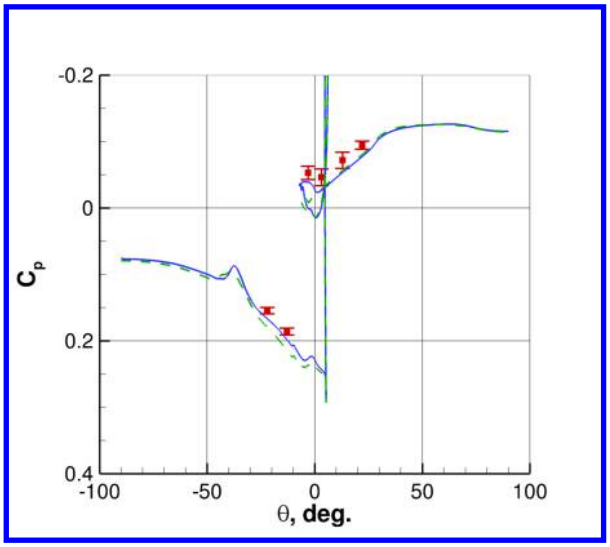

(d) $x = 2921$ mm

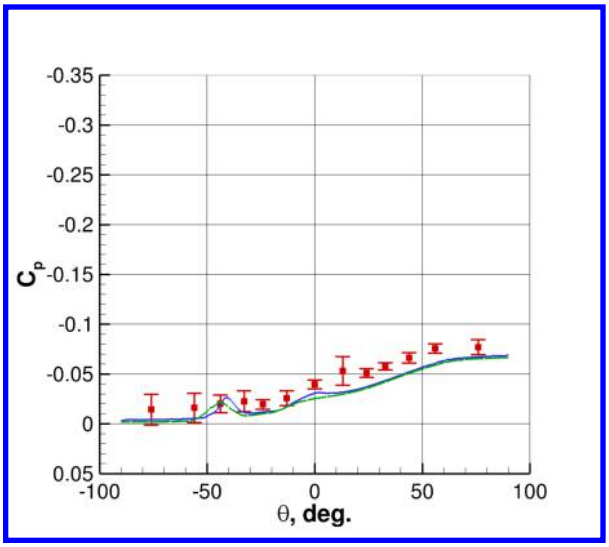

(e) $x = 3556$ mm

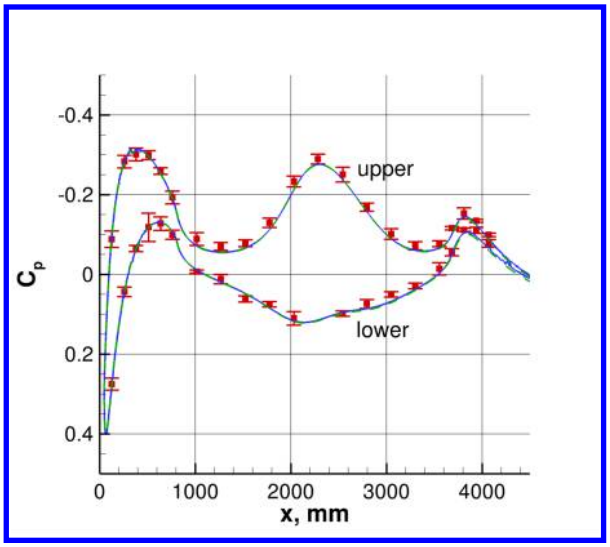

(f) $y = -76.2$ mm

Figure 5. Surface pressure coefficients on fuselage, $\alpha = 7.5°$.

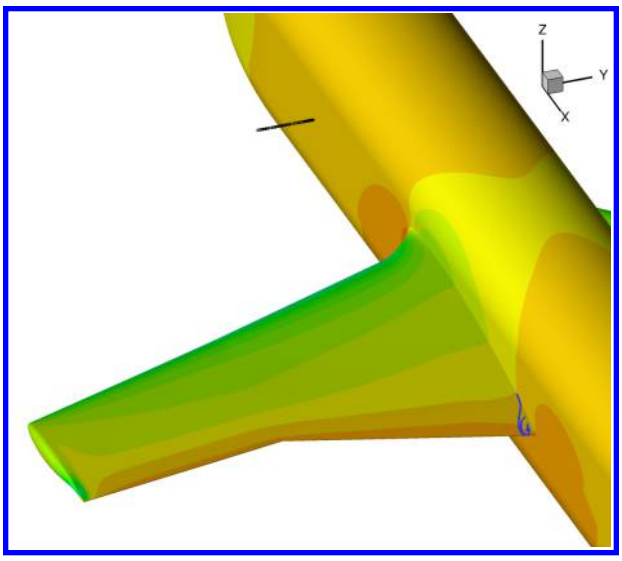

(a) Location of profiles

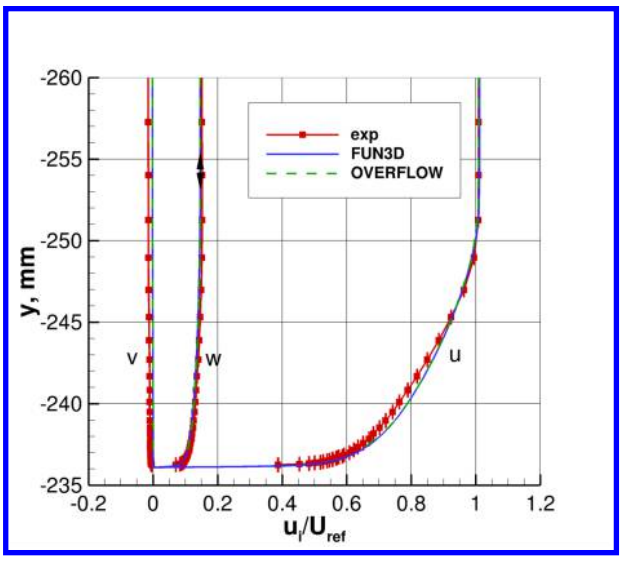

(b) Velocity profiles

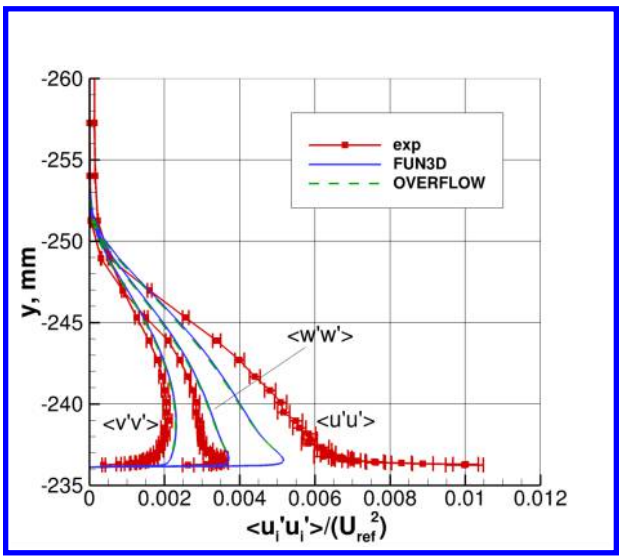

(c) Turbulent normal stress profiles

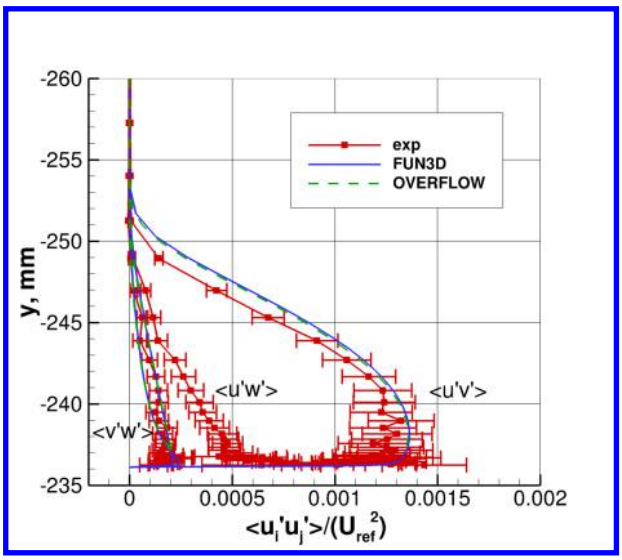

(d) Turbulent shear stress profiles

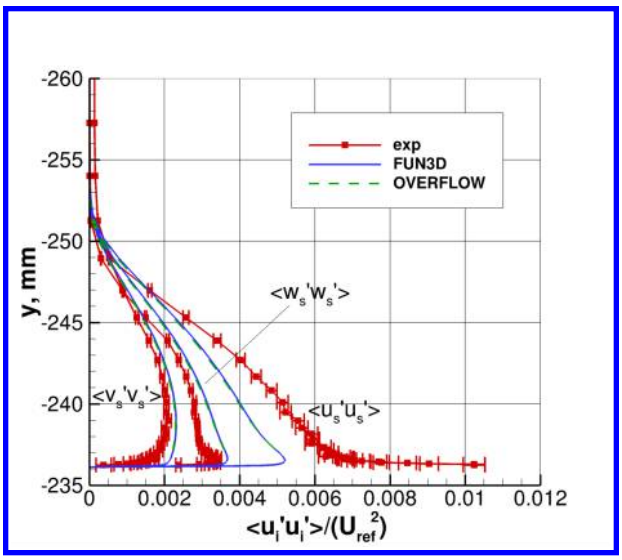

(e) Turbulent normal stress profiles in streamwise axis system

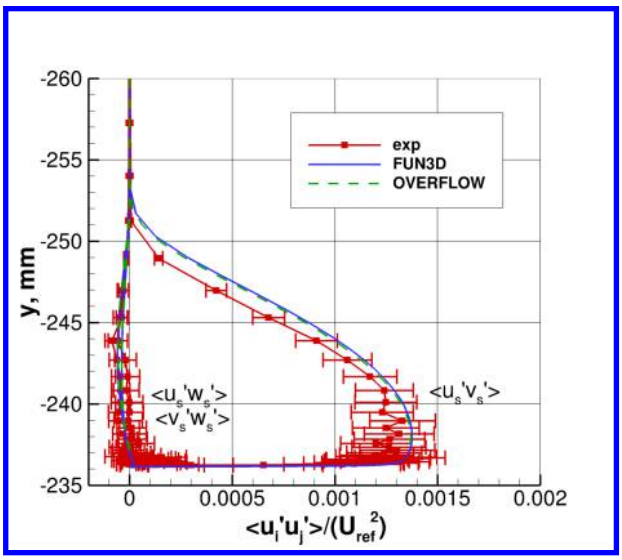

(f) Turbulent shear stress profiles in streamwise axis system

Figure 6. Profiles upstream on side of fuselage nose, $x = 1168.4$ mm, $z = 0$ mm, $\alpha = 5°$.

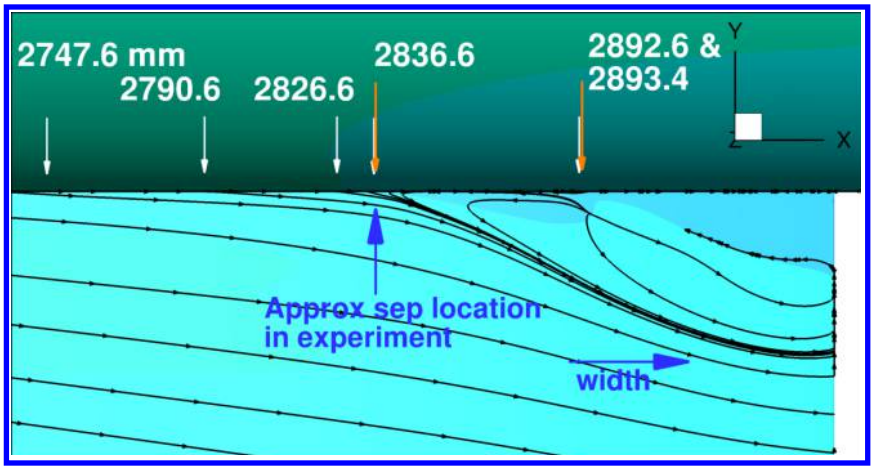

(a) $\alpha = 7.5°$

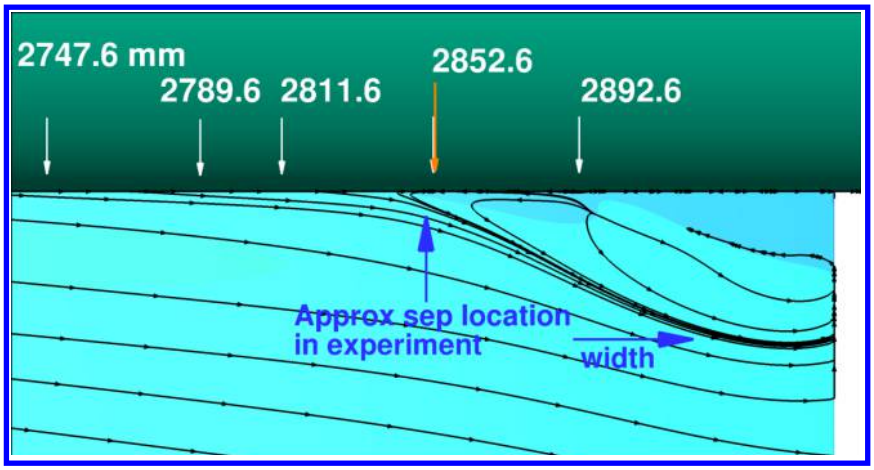

(b) $\alpha = 5°$

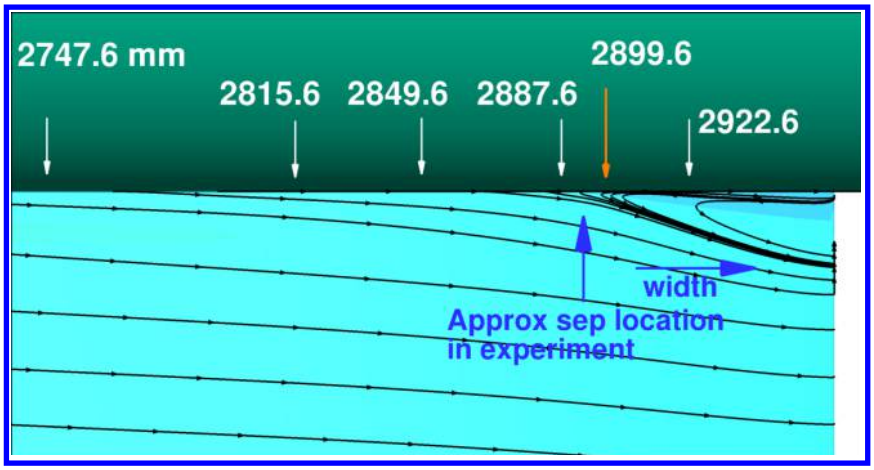

(c) $\alpha = -2.5°$

Figure 7. Planar data locations from experiment that are plotted in the current paper; shorter white arrows represent LDV stations, longer orange arrows represent PIV stations; streamlines from FUN3D show computed separation; blue arrows indicate oil flow separation size.

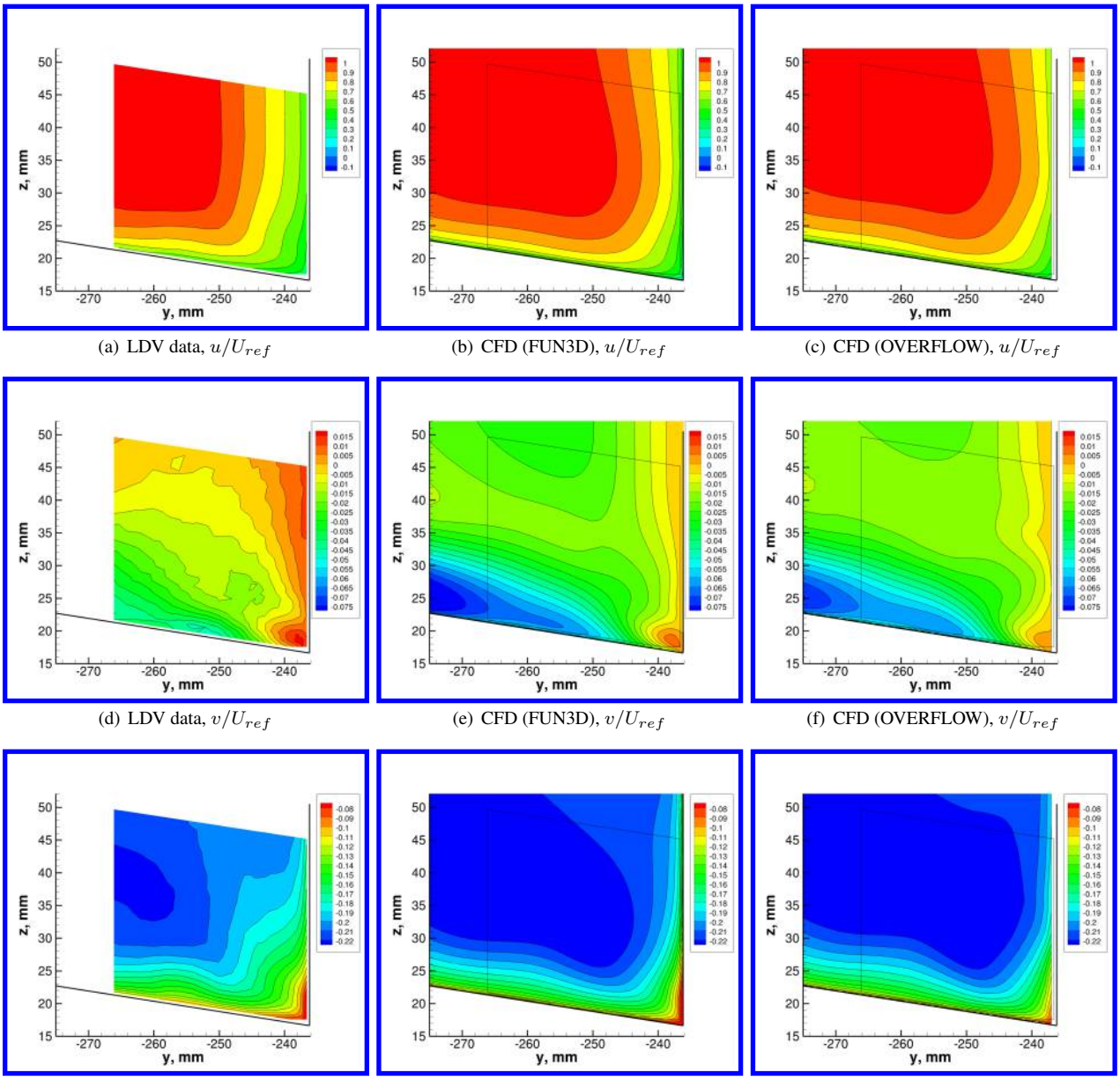

(a) LDV data, u/U_{ref} (b) CFD (FUN3D), u/U_{ref} (c) CFD (OVERFLOW), u/U_{ref}

(d) LDV data, v/U_{ref} (e) CFD (FUN3D), v/U_{ref} (f) CFD (OVERFLOW), v/U_{ref}

(g) LDV data, w/U_{ref} (h) CFD (FUN3D), w/U_{ref} (i) CFD (OVERFLOW), w/U_{ref}

Figure 8. Contours of velocity components, $x = 2747.6$ mm, $\alpha = 7.5°$.

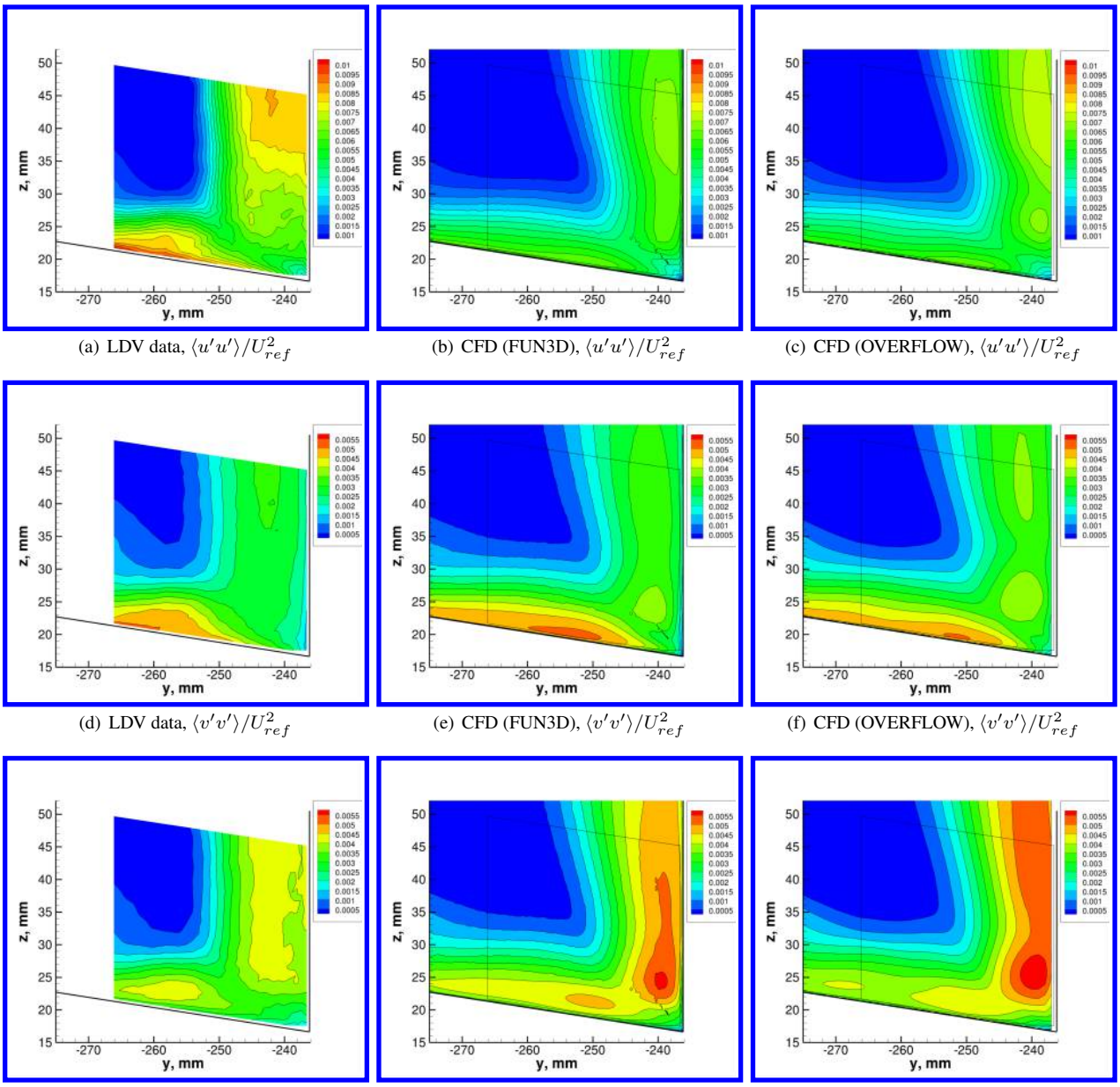

(a) LDV data, $\langle u'u' \rangle / U_{ref}^2$ (b) CFD (FUN3D), $\langle u'u' \rangle / U_{ref}^2$ (c) CFD (OVERFLOW), $\langle u'u' \rangle / U_{ref}^2$

(d) LDV data, $\langle v'v' \rangle / U_{ref}^2$ (e) CFD (FUN3D), $\langle v'v' \rangle / U_{ref}^2$ (f) CFD (OVERFLOW), $\langle v'v' \rangle / U_{ref}^2$

(g) LDV data, $\langle w'w' \rangle / U_{ref}^2$ (h) CFD (FUN3D), $\langle w'w' \rangle / U_{ref}^2$ (i) CFD (OVERFLOW), $\langle w'w' \rangle / U_{ref}^2$

Figure 9. Contours of Reynolds normal stresses, $x = 2747.6$ mm, $\alpha = 7.5°$.

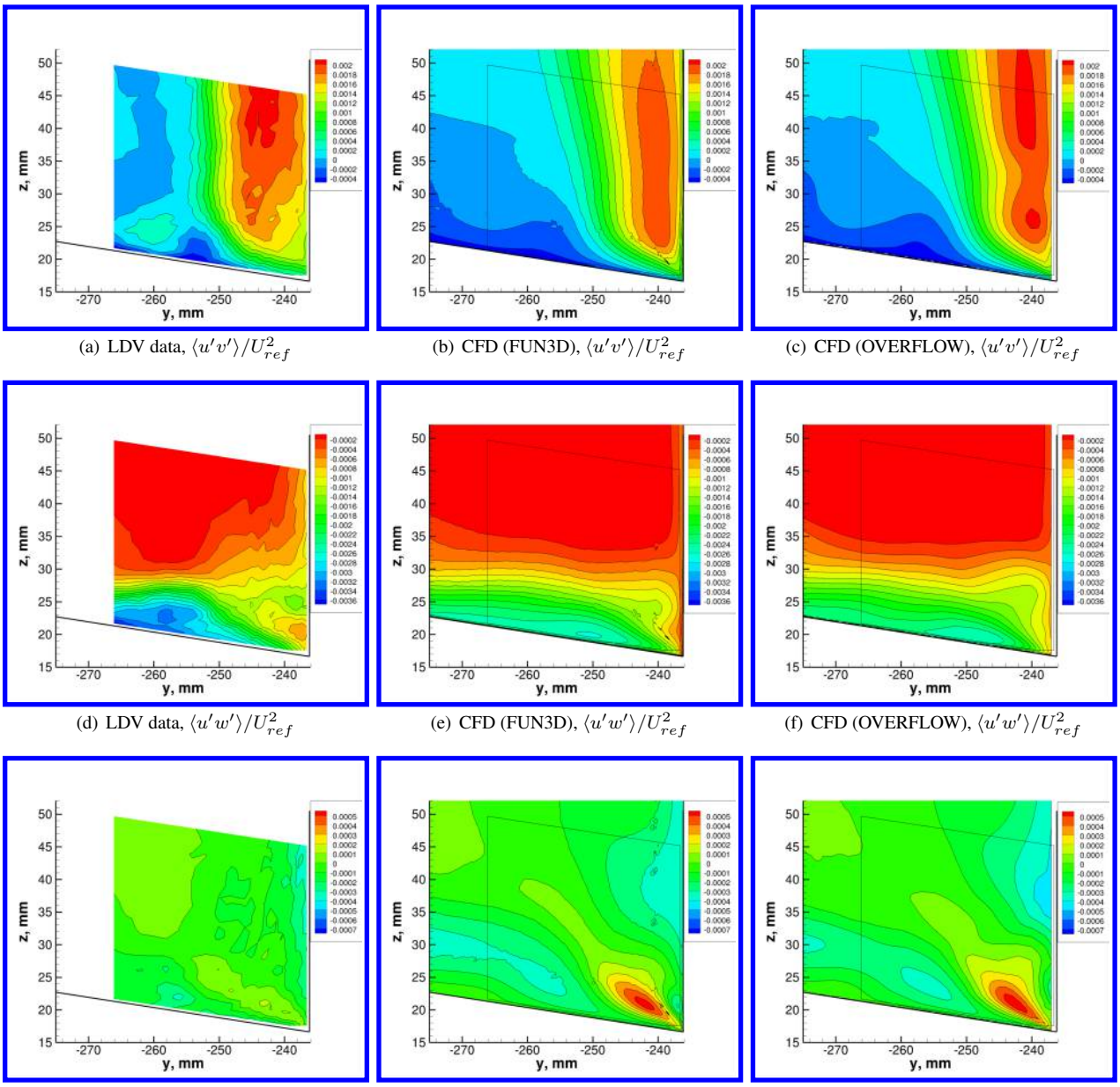

(a) LDV data, $\langle u'v' \rangle / U_{ref}^2$ (b) CFD (FUN3D), $\langle u'v' \rangle / U_{ref}^2$ (c) CFD (OVERFLOW), $\langle u'v' \rangle / U_{ref}^2$

(d) LDV data, $\langle u'w' \rangle / U_{ref}^2$ (e) CFD (FUN3D), $\langle u'w' \rangle / U_{ref}^2$ (f) CFD (OVERFLOW), $\langle u'w' \rangle / U_{ref}^2$

(g) LDV data, $\langle v'w' \rangle / U_{ref}^2$ (h) CFD (FUN3D), $\langle v'w' \rangle / U_{ref}^2$ (i) CFD (OVERFLOW), $\langle v'w' \rangle / U_{ref}^2$

Figure 10. Contours of Reynolds shear stresses, $x = 2747.6$ mm, $\alpha = 7.5°$.

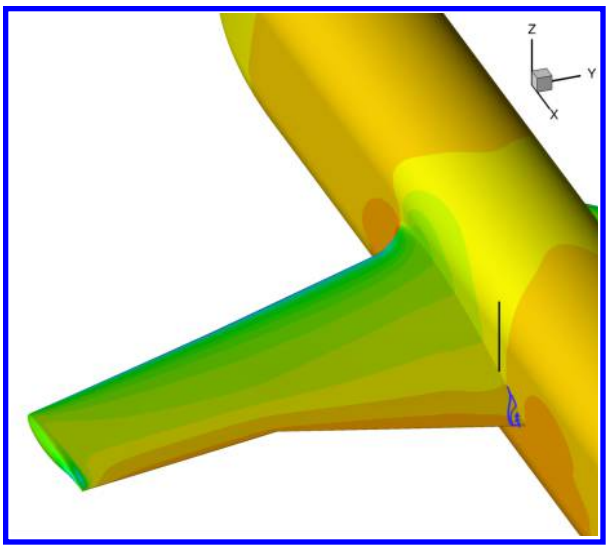

(a) Location of profiles

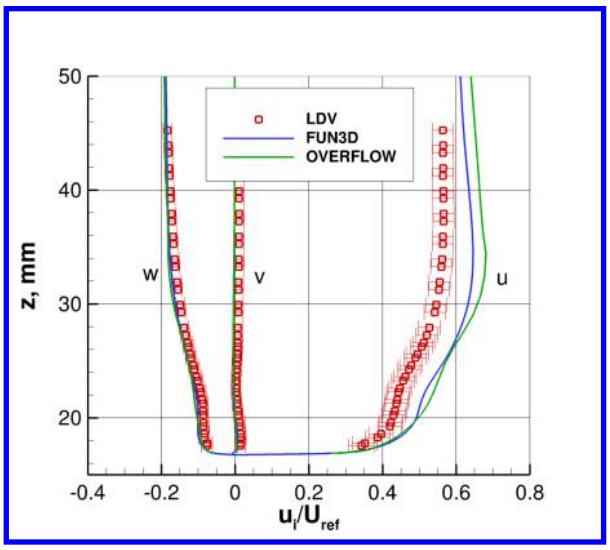

(b) Velocity profiles

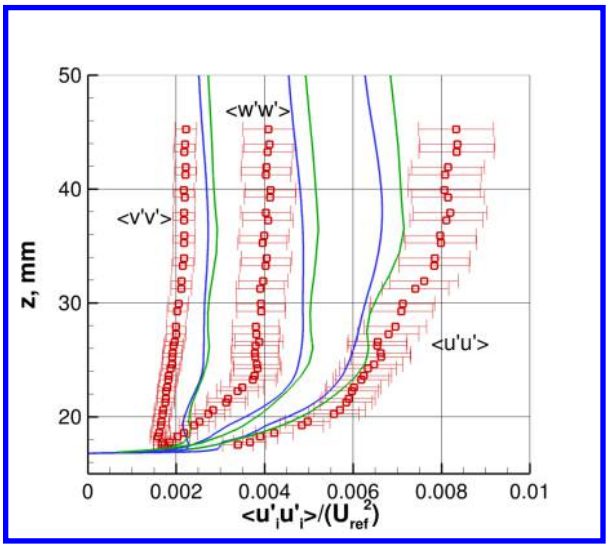

(c) Turbulent normal stress profiles

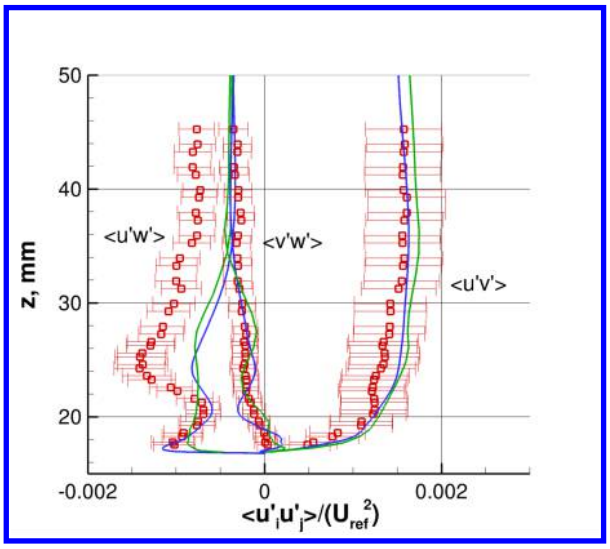

(d) Turbulent shear stress profiles

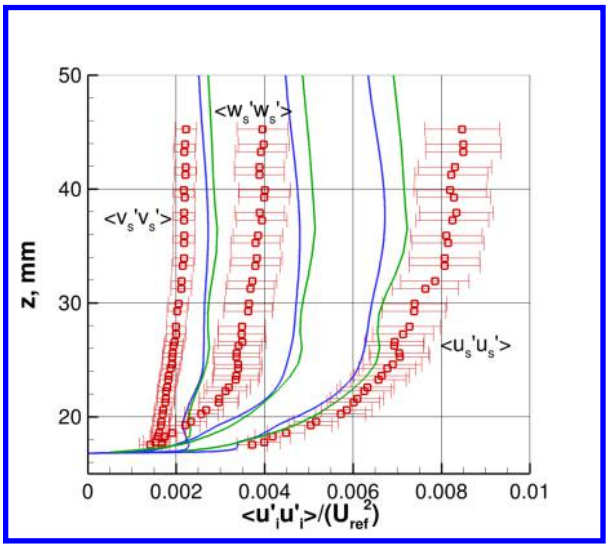

(e) Turbulent normal stress profiles in streamwise axis system

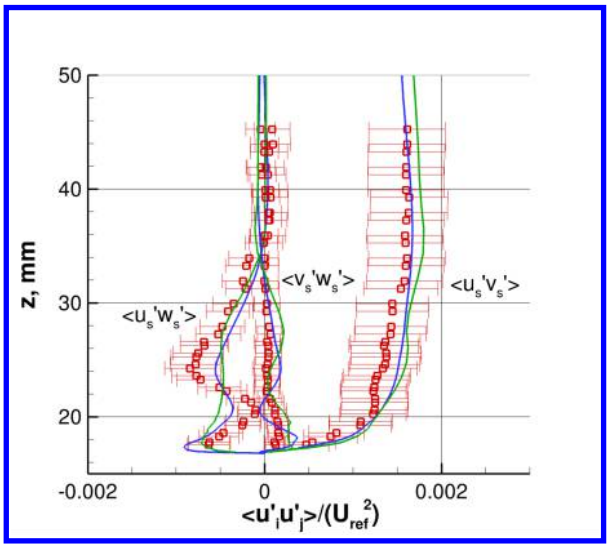

(f) Turbulent shear stress profiles in streamwise axis system

Figure 11. Profiles along $x = 2747.6$ mm and $y = -237.1$ mm, $\alpha = 7.5°$.

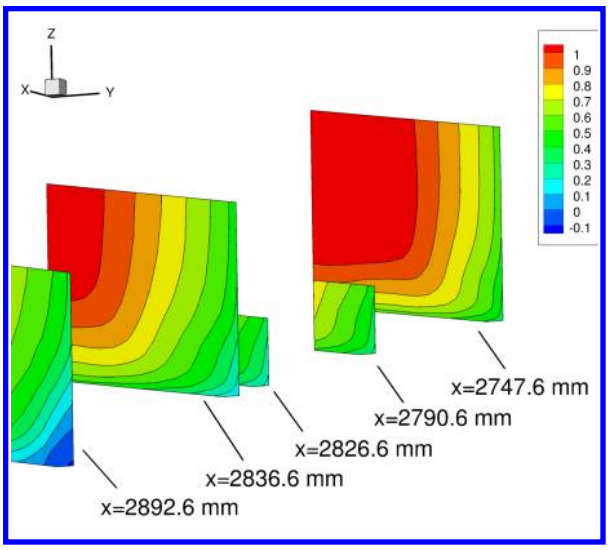

(a) LDV data, u/U_{ref}

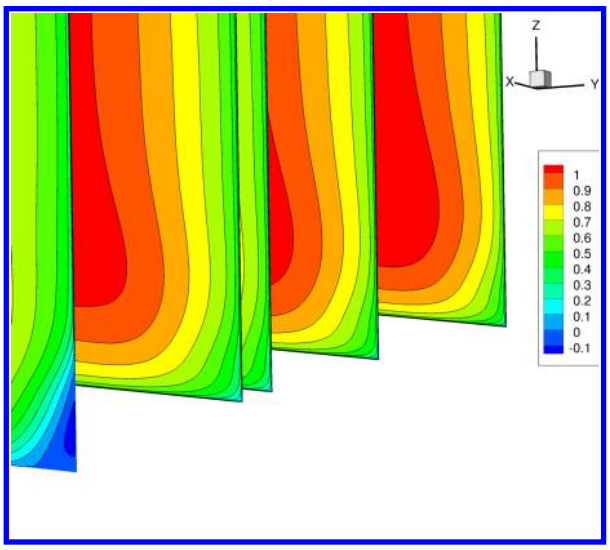

(b) CFD (FUN3D), u/U_{ref}

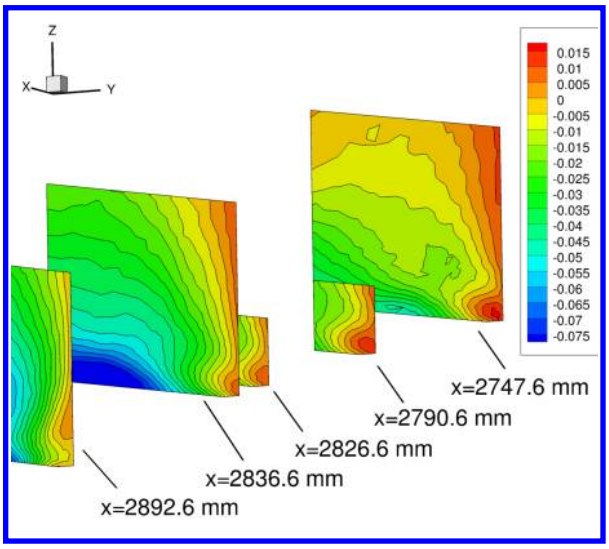

(c) LDV data, v/U_{ref}

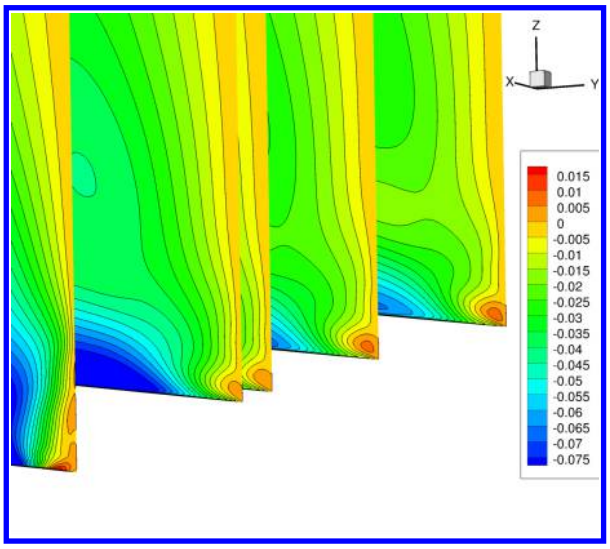

(d) CFD (FUN3D), v/U_{ref}

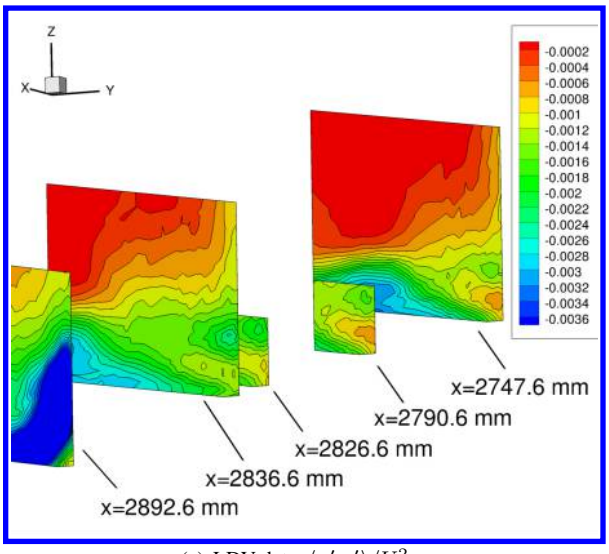

(e) LDV data, $\langle u'w' \rangle / U_{ref}^2$

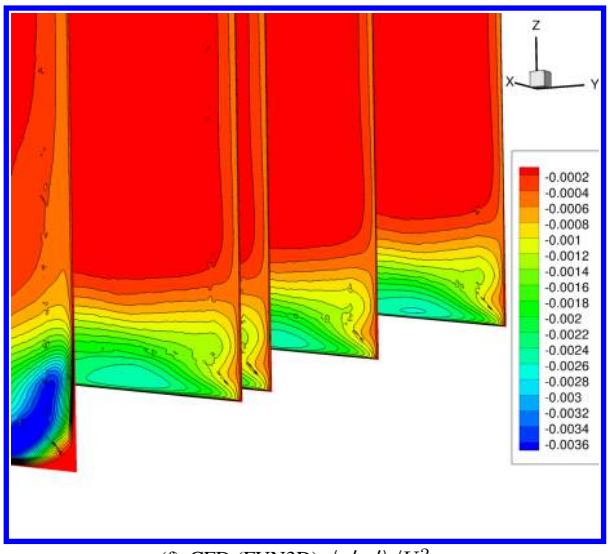

(f) CFD (FUN3D), $\langle u'w' \rangle / U_{ref}^2$

Figure 12. Progression of selected contours of interest, $\alpha = 7.5°$.

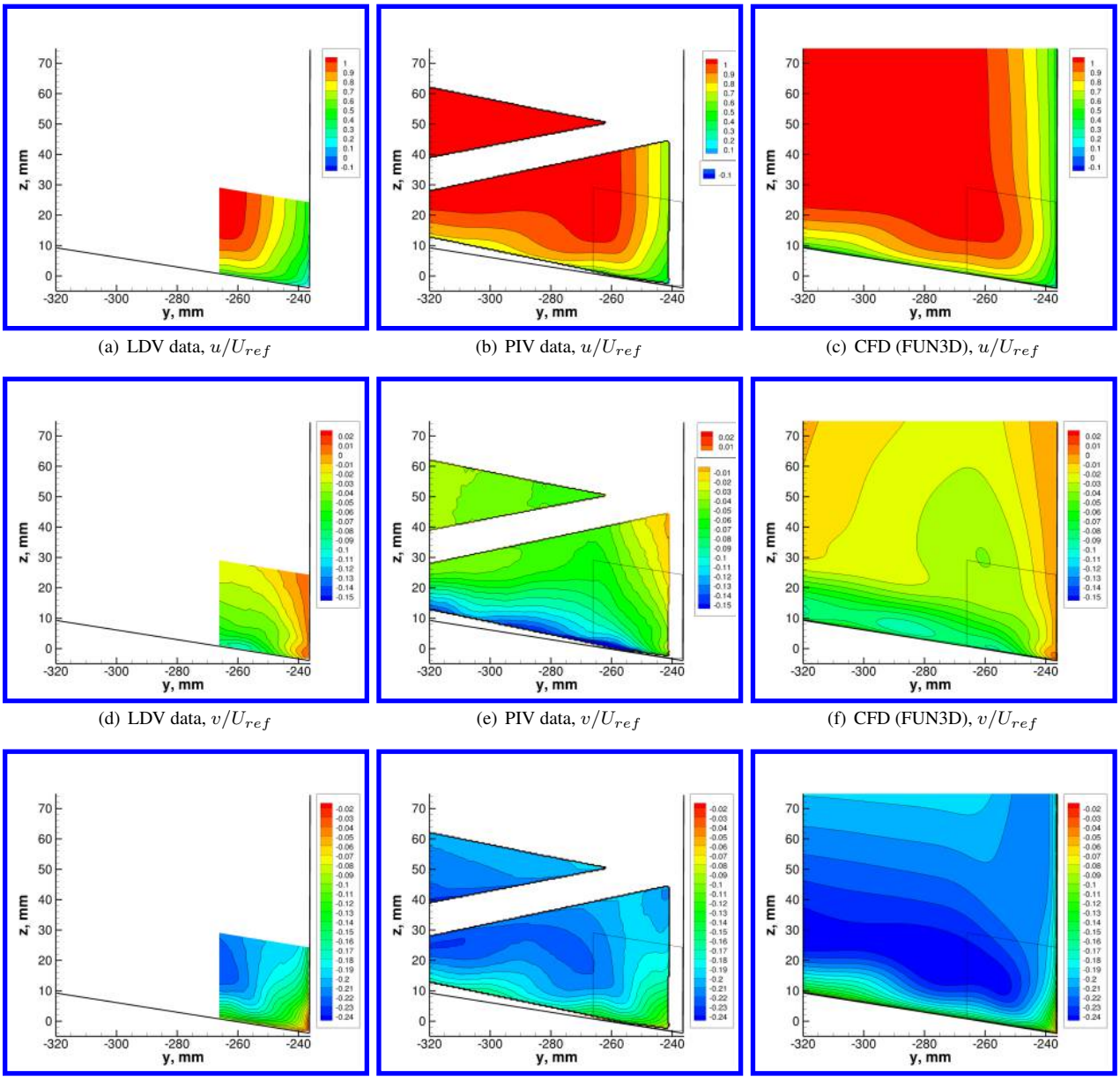

(a) LDV data, u/U_{ref} (b) PIV data, u/U_{ref} (c) CFD (FUN3D), u/U_{ref}

(d) LDV data, v/U_{ref} (e) PIV data, v/U_{ref} (f) CFD (FUN3D), v/U_{ref}

(g) LDV data, w/U_{ref} (h) PIV data, w/U_{ref} (i) CFD (FUN3D), w/U_{ref}

Figure 13. Contours of velocity components near separation, $x = 2836.6$ mm, $\alpha = 7.5°$.

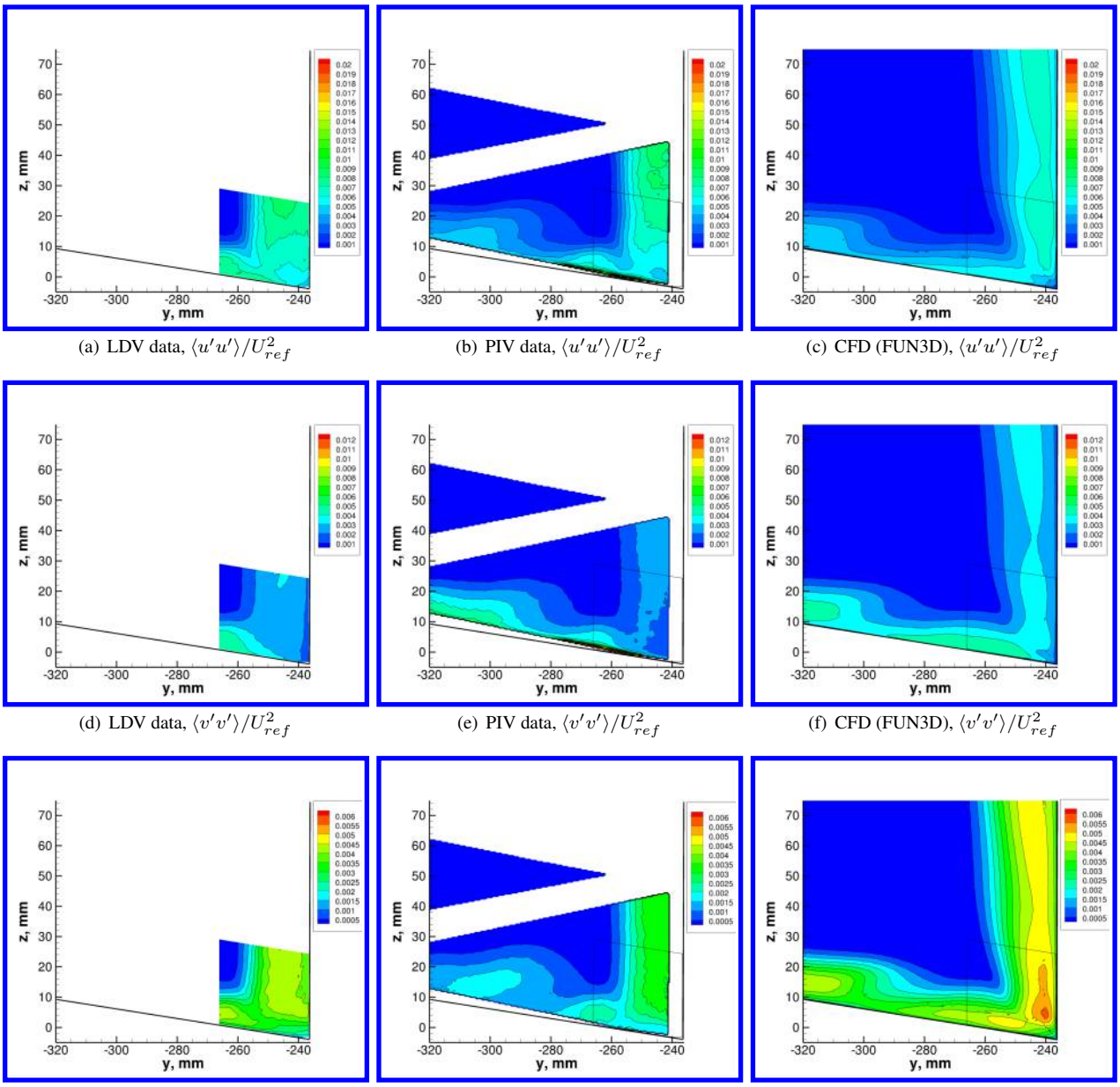

(a) LDV data, $\langle u'u' \rangle / U_{ref}^2$ (b) PIV data, $\langle u'u' \rangle / U_{ref}^2$ (c) CFD (FUN3D), $\langle u'u' \rangle / U_{ref}^2$

(d) LDV data, $\langle v'v' \rangle / U_{ref}^2$ (e) PIV data, $\langle v'v' \rangle / U_{ref}^2$ (f) CFD (FUN3D), $\langle v'v' \rangle / U_{ref}^2$

(g) LDV data, $\langle w'w' \rangle / U_{ref}^2$ (h) PIV data, $\langle w'w' \rangle / U_{ref}^2$ (i) CFD (FUN3D), $\langle w'w' \rangle / U_{ref}^2$

Figure 14. Contours of Reynolds normal stresses near separation, $x = 2836.6$ mm, $\alpha = 7.5°$.

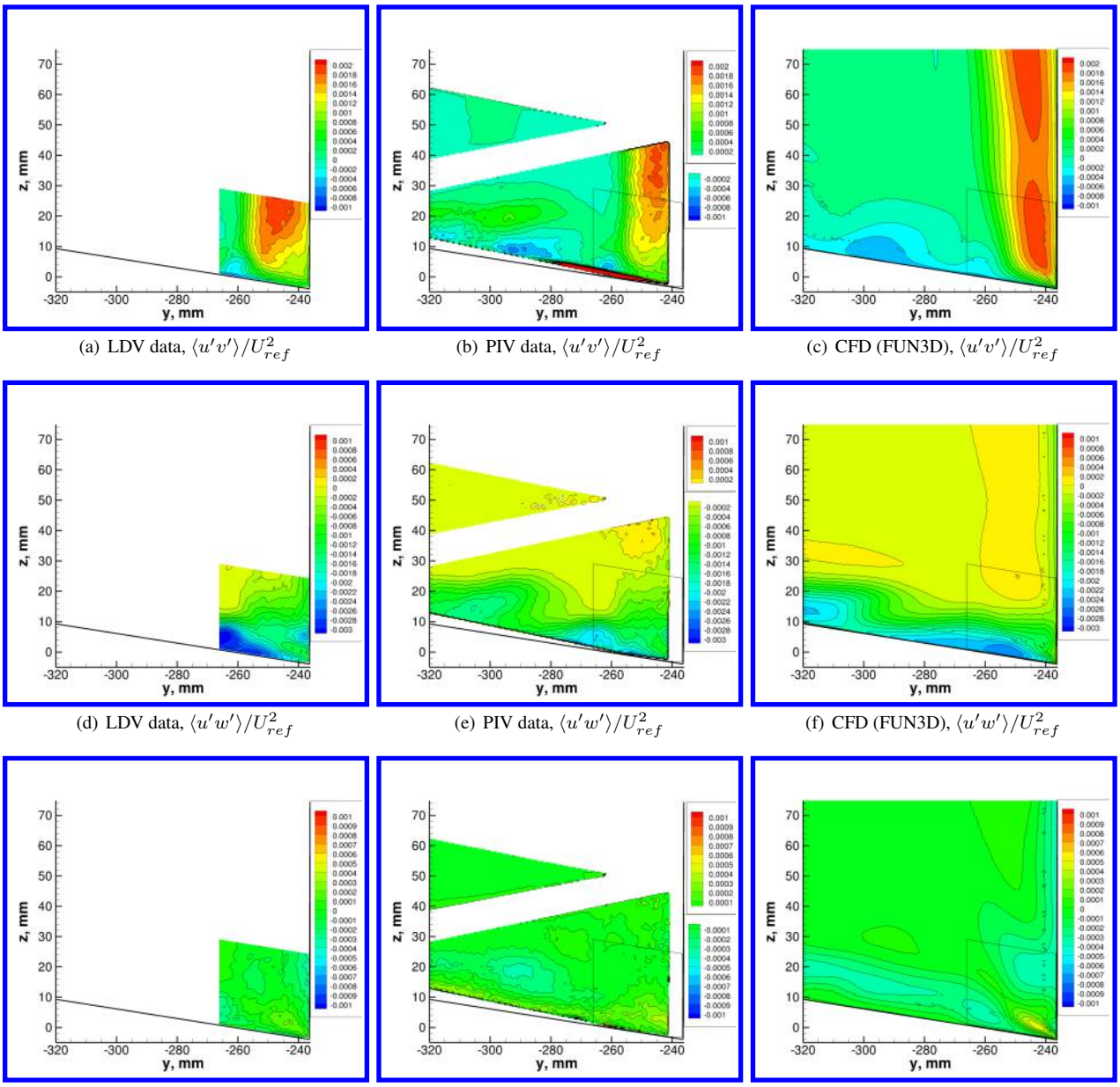

(a) LDV data, $\langle u'v' \rangle / U_{ref}^2$ (b) PIV data, $\langle u'v' \rangle / U_{ref}^2$ (c) CFD (FUN3D), $\langle u'v' \rangle / U_{ref}^2$

(d) LDV data, $\langle u'w' \rangle / U_{ref}^2$ (e) PIV data, $\langle u'w' \rangle / U_{ref}^2$ (f) CFD (FUN3D), $\langle u'w' \rangle / U_{ref}^2$

(g) LDV data, $\langle v'w' \rangle / U_{ref}^2$ (h) PIV data, $\langle v'w' \rangle / U_{ref}^2$ (i) CFD (FUN3D), $\langle v'w' \rangle / U_{ref}^2$

Figure 15. Contours of Reynolds shear stresses near separation, $x = 2836.6$ mm, $\alpha = 7.5°$.

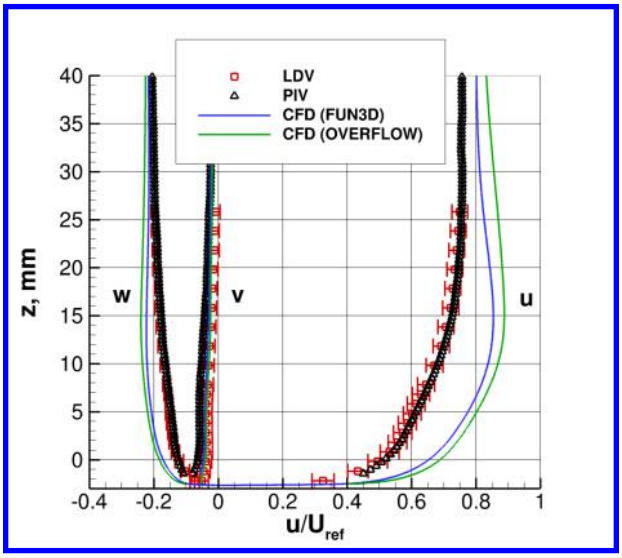

(a) Velocity profiles

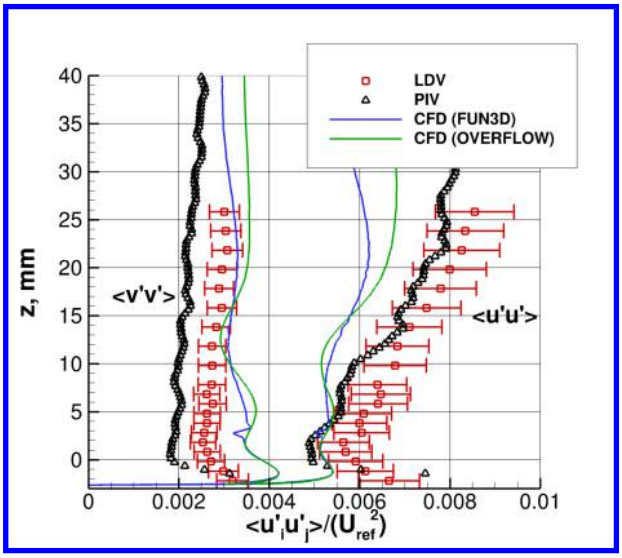

(b) Turbulence profiles (part 1)

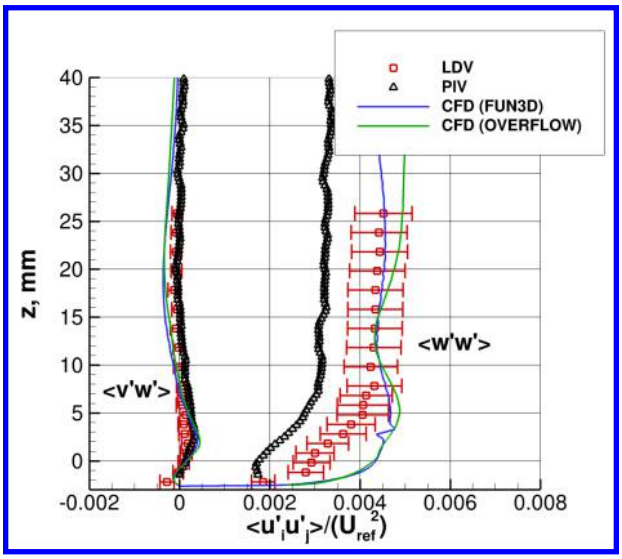

(c) Turbulence profiles (part 2)

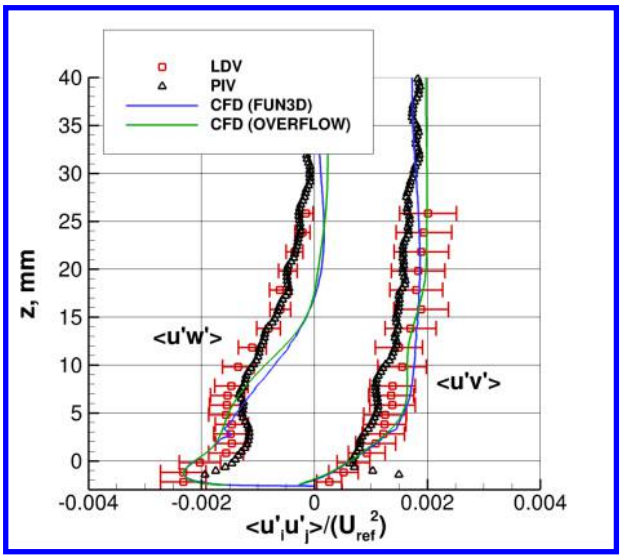

(d) Turbulence profiles (part 3)

Figure 16. Profiles along $x = 2836.6$ mm and $y = -246.1$ mm, $\alpha = 7.5°$.

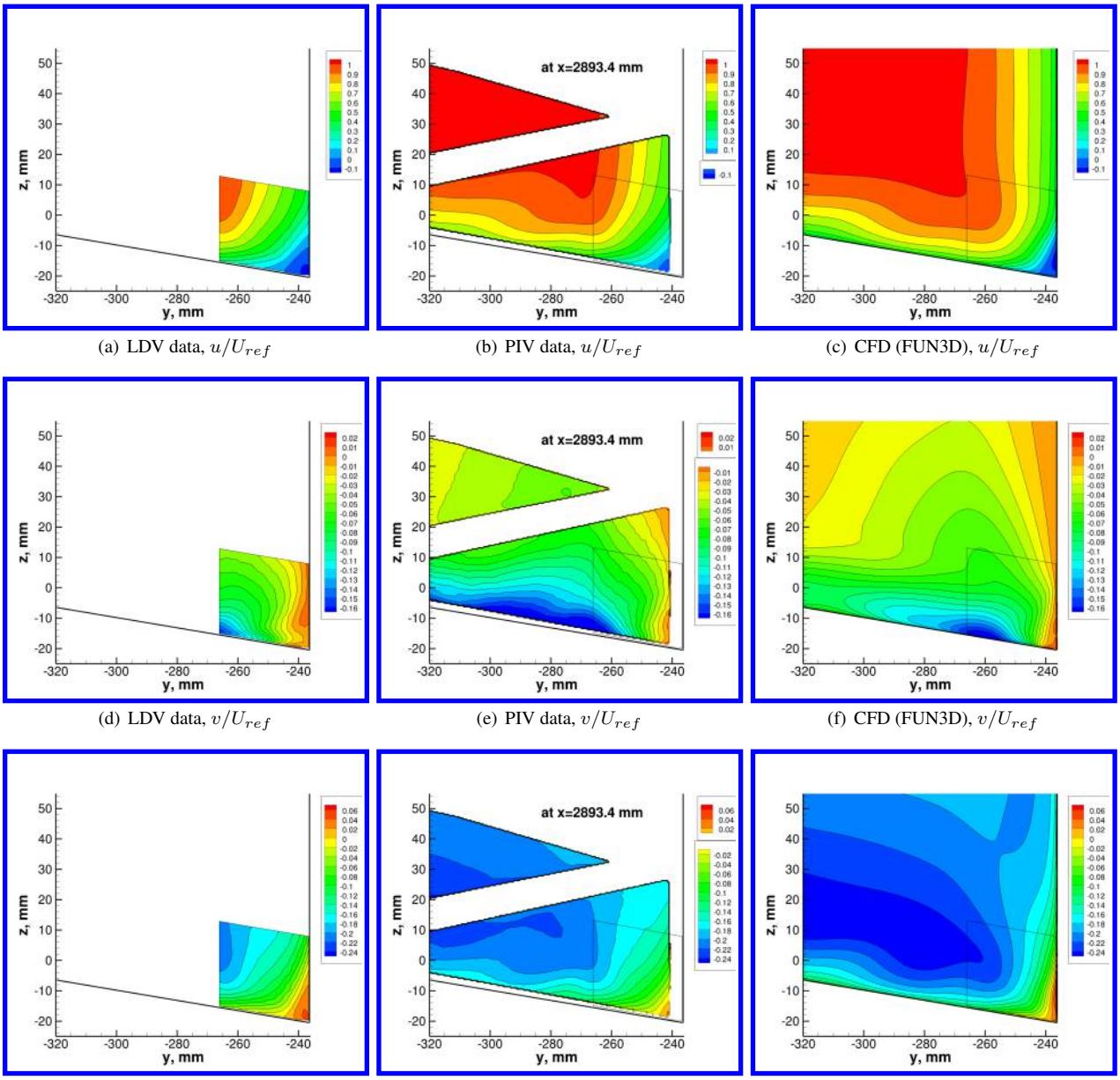

(a) LDV data, u/U_{ref} (b) PIV data, u/U_{ref} (c) CFD (FUN3D), u/U_{ref}

(d) LDV data, v/U_{ref} (e) PIV data, v/U_{ref} (f) CFD (FUN3D), v/U_{ref}

(g) LDV data, w/U_{ref} (h) PIV data, w/U_{ref} (i) CFD (FUN3D), w/U_{ref}

Figure 17. Contours of velocity components post separation, $x = 2892.6$ mm, $\alpha = 7.5°$.

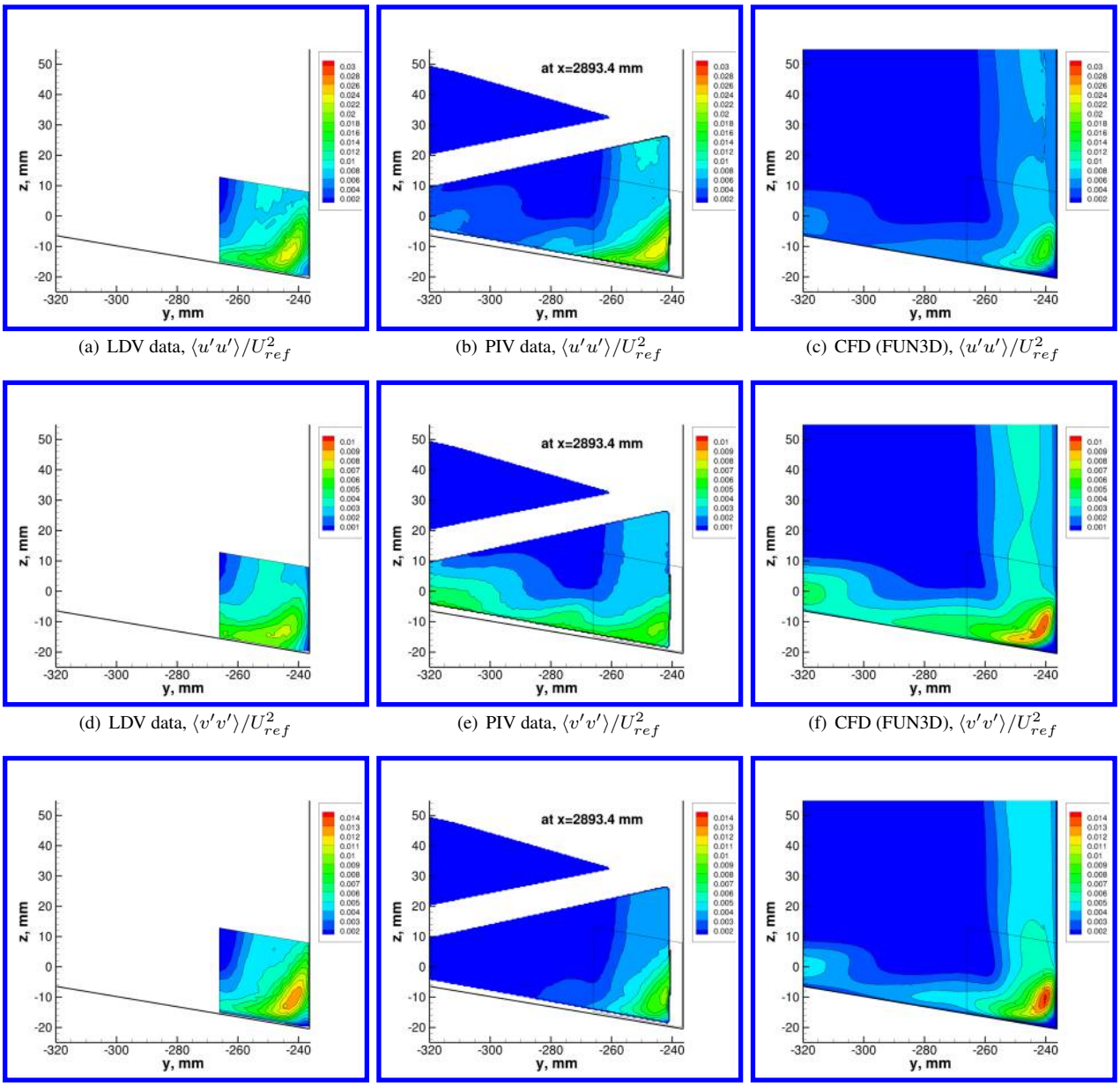

(a) LDV data, $\langle u'u' \rangle / U_{ref}^2$ (b) PIV data, $\langle u'u' \rangle / U_{ref}^2$ (c) CFD (FUN3D), $\langle u'u' \rangle / U_{ref}^2$

(d) LDV data, $\langle v'v' \rangle / U_{ref}^2$ (e) PIV data, $\langle v'v' \rangle / U_{ref}^2$ (f) CFD (FUN3D), $\langle v'v' \rangle / U_{ref}^2$

(g) LDV data, $\langle w'w' \rangle / U_{ref}^2$ (h) PIV data, $\langle w'w' \rangle / U_{ref}^2$ (i) CFD (FUN3D), $\langle w'w' \rangle / U_{ref}^2$

Figure 18. Contours of Reynolds normal stresses post separation, $x = 2892.6$ mm, $\alpha = 7.5°$.

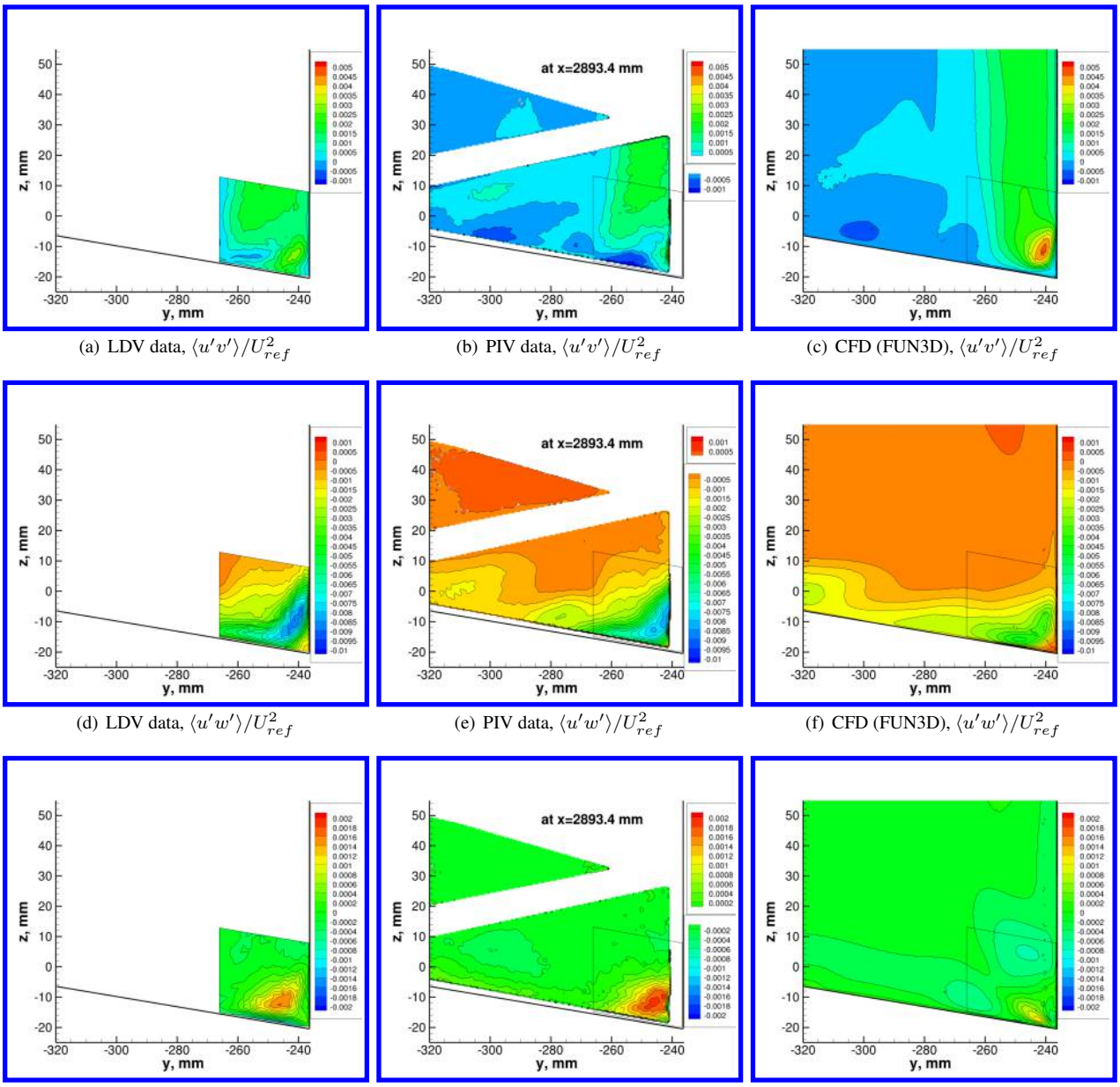

(a) LDV data, $\langle u'v' \rangle / U_{ref}^2$ (b) PIV data, $\langle u'v' \rangle / U_{ref}^2$ (c) CFD (FUN3D), $\langle u'v' \rangle / U_{ref}^2$

(d) LDV data, $\langle u'w' \rangle / U_{ref}^2$ (e) PIV data, $\langle u'w' \rangle / U_{ref}^2$ (f) CFD (FUN3D), $\langle u'w' \rangle / U_{ref}^2$

(g) LDV data, $\langle v'w' \rangle / U_{ref}^2$ (h) PIV data, $\langle v'w' \rangle / U_{ref}^2$ (i) CFD (FUN3D), $\langle v'w' \rangle / U_{ref}^2$

Figure 19. Contours of Reynolds shear stresses post separation, $x = 2892.6$ mm, $\alpha = 7.5°$.

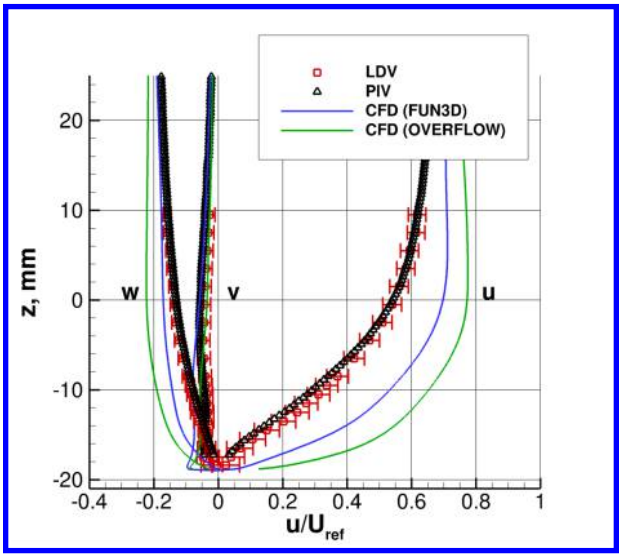

(a) Velocity profiles

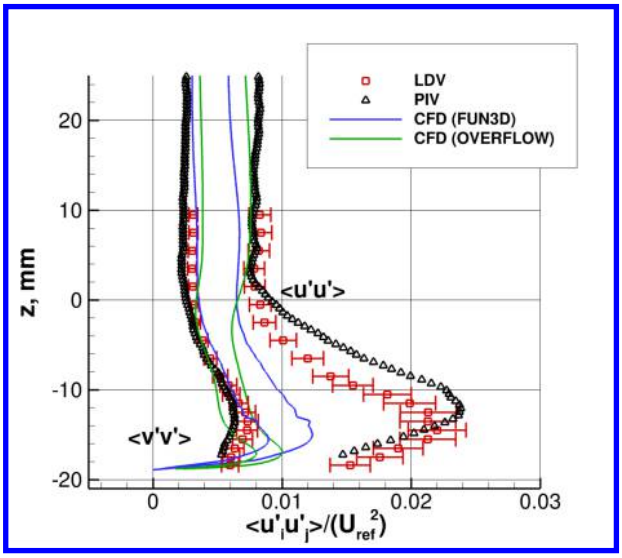

(b) Turbulence profiles (part 1)

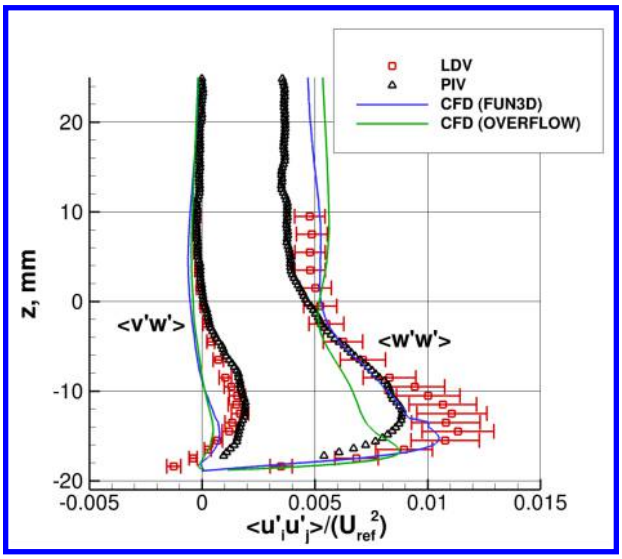

(c) Turbulence profiles (part 2)

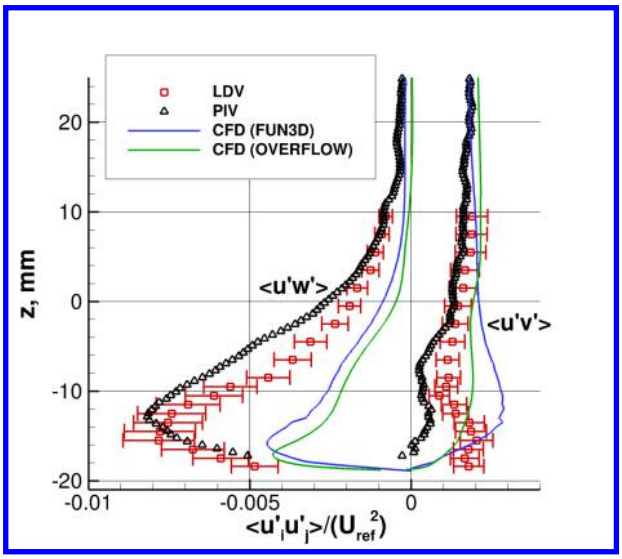

(d) Turbulence profiles (part 3)

Figure 20. Profiles along $x = 2892.6$ mm (PIV at 2893.4 mm) and $y = -246.1$ mm, $\alpha = 7.5°$.

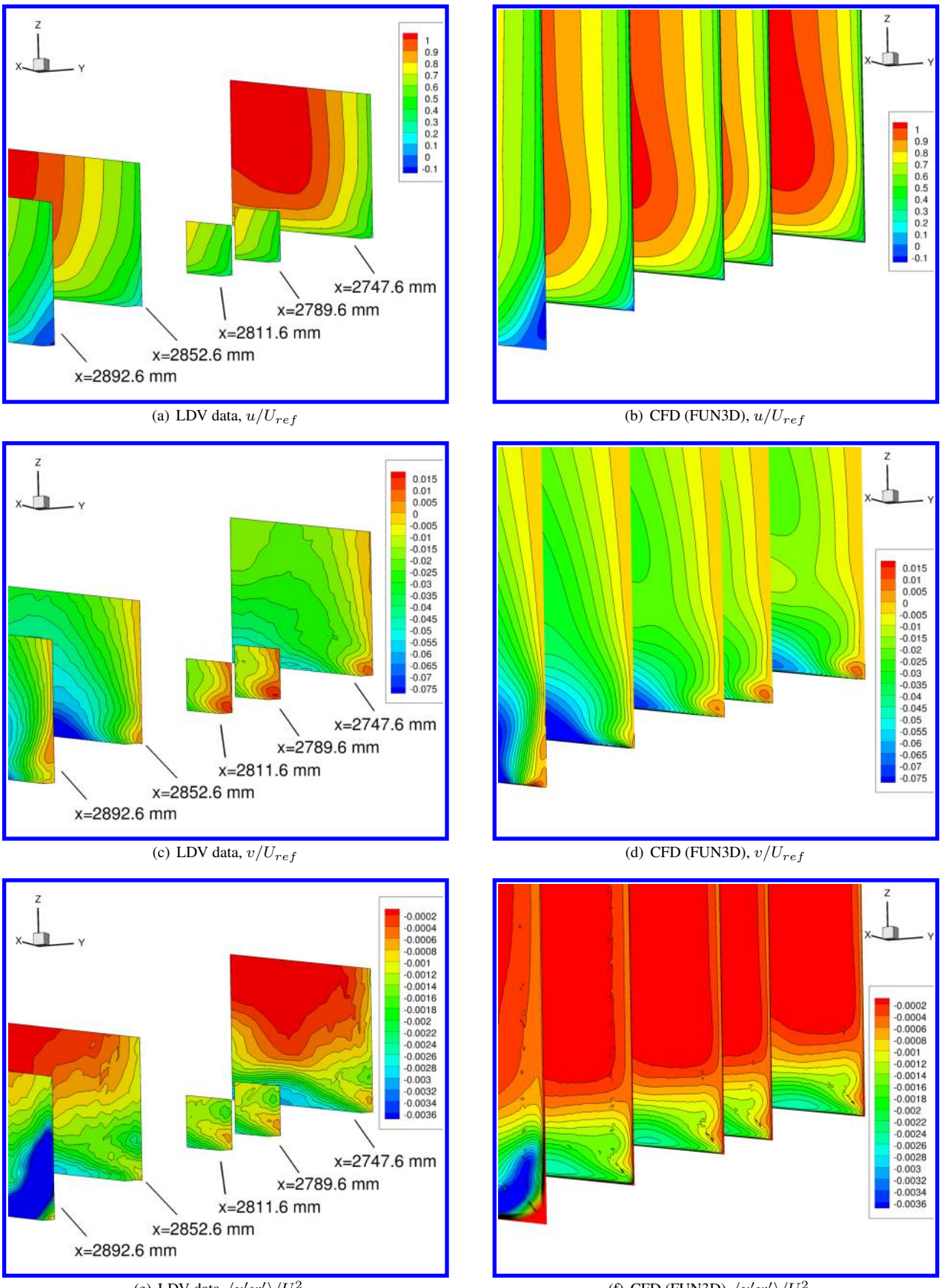

(a) LDV data, u/U_{ref}

(b) CFD (FUN3D), u/U_{ref}

(c) LDV data, v/U_{ref}

(d) CFD (FUN3D), v/U_{ref}

(e) LDV data, $\langle u'w' \rangle / U_{ref}^2$

(f) CFD (FUN3D), $\langle u'w' \rangle / U_{ref}^2$

Figure 21. Progression of selected contours of interest, $\alpha = 5^\circ$.

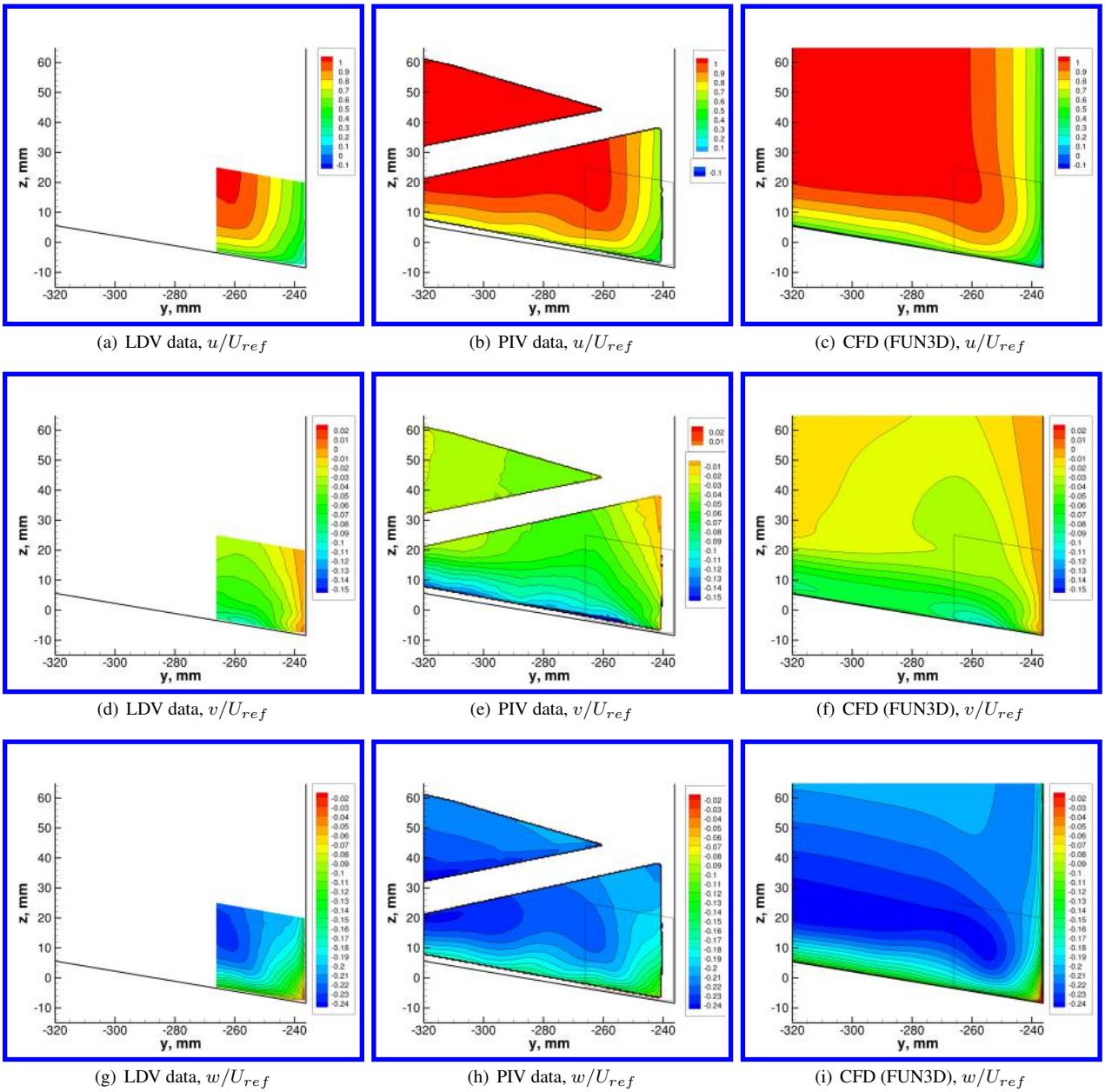

(a) LDV data, u/U_{ref} (b) PIV data, u/U_{ref} (c) CFD (FUN3D), u/U_{ref}

(d) LDV data, v/U_{ref} (e) PIV data, v/U_{ref} (f) CFD (FUN3D), v/U_{ref}

(g) LDV data, w/U_{ref} (h) PIV data, w/U_{ref} (i) CFD (FUN3D), w/U_{ref}

Figure 22. Contours of velocity components near separation, $x = 2852.6$ mm, $\alpha = 5°$.

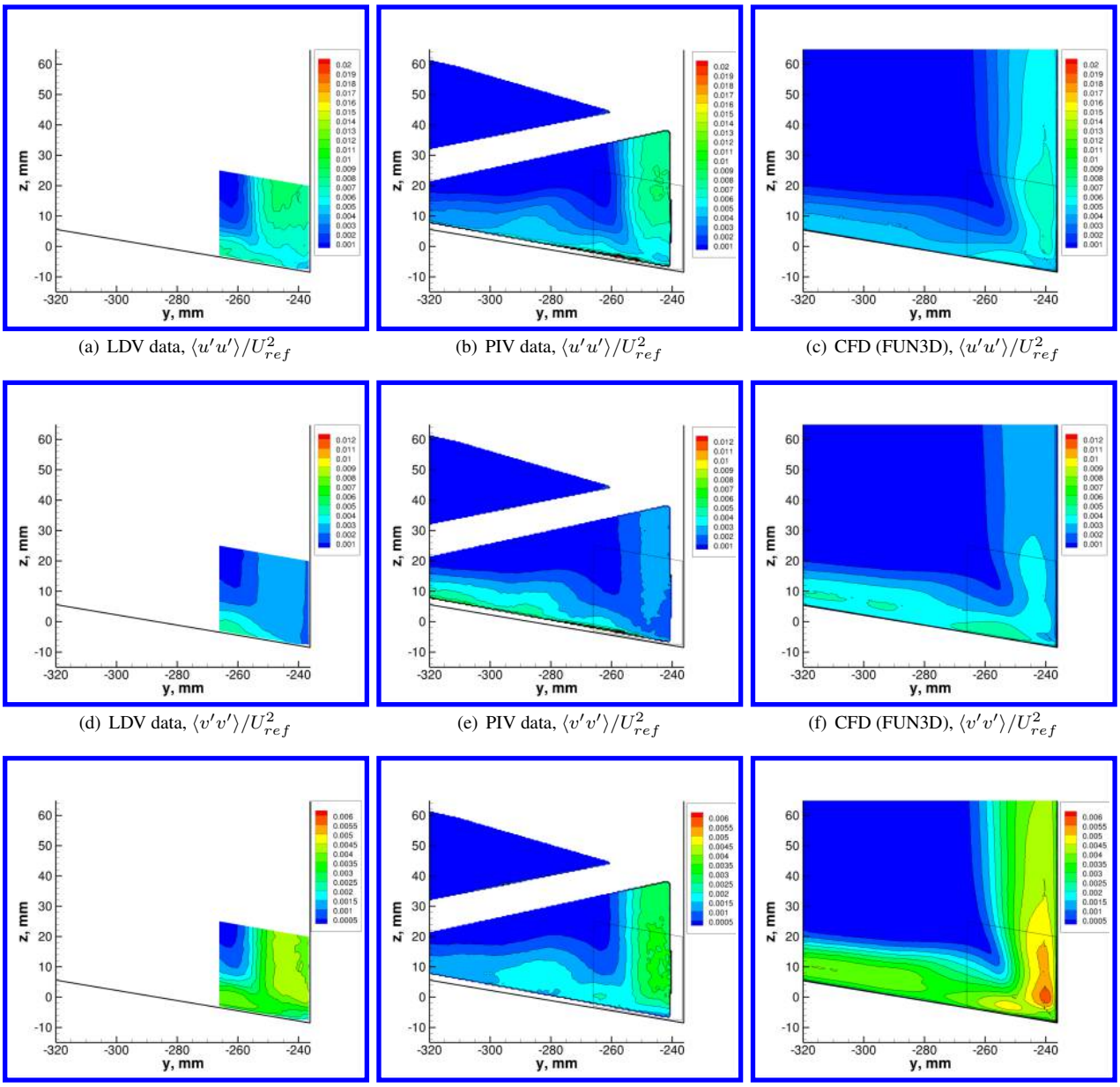

(a) LDV data, $\langle u'u' \rangle / U_{ref}^2$ (b) PIV data, $\langle u'u' \rangle / U_{ref}^2$ (c) CFD (FUN3D), $\langle u'u' \rangle / U_{ref}^2$

(d) LDV data, $\langle v'v' \rangle / U_{ref}^2$ (e) PIV data, $\langle v'v' \rangle / U_{ref}^2$ (f) CFD (FUN3D), $\langle v'v' \rangle / U_{ref}^2$

(g) LDV data, $\langle w'w' \rangle / U_{ref}^2$ (h) PIV data, $\langle w'w' \rangle / U_{ref}^2$ (i) CFD (FUN3D), $\langle w'w' \rangle / U_{ref}^2$

Figure 23. Contours of Reynolds normal stresses near separation, $x = 2852.6$ mm, $\alpha = 5°$.

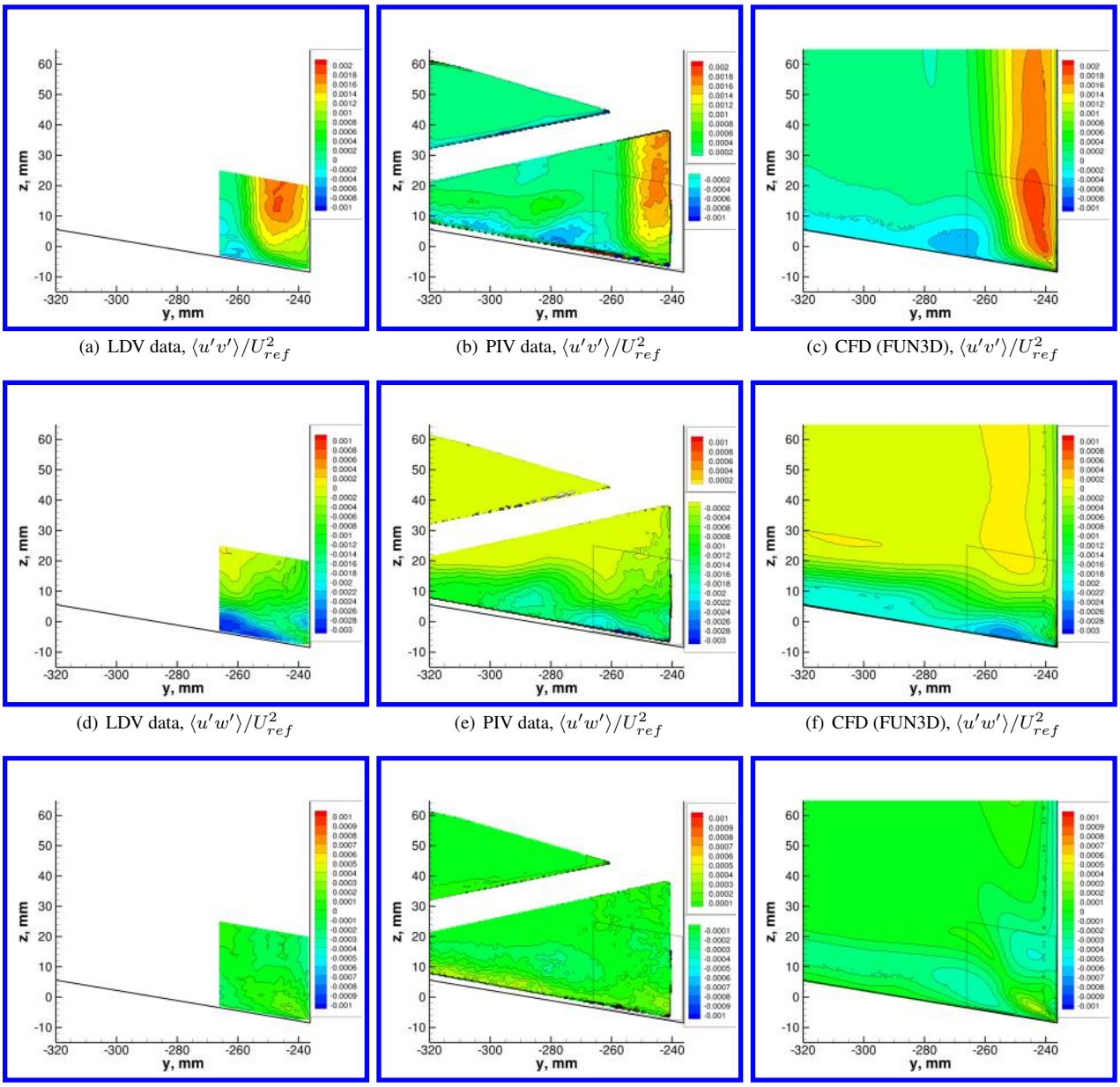

(a) LDV data, $\langle u'v' \rangle / U_{ref}^2$ (b) PIV data, $\langle u'v' \rangle / U_{ref}^2$ (c) CFD (FUN3D), $\langle u'v' \rangle / U_{ref}^2$

(d) LDV data, $\langle u'w' \rangle / U_{ref}^2$ (e) PIV data, $\langle u'w' \rangle / U_{ref}^2$ (f) CFD (FUN3D), $\langle u'w' \rangle / U_{ref}^2$

(g) LDV data, $\langle v'w' \rangle / U_{ref}^2$ (h) PIV data, $\langle v'w' \rangle / U_{ref}^2$ (i) CFD (FUN3D), $\langle v'w' \rangle / U_{ref}^2$

Figure 24. Contours of Reynolds shear stresses near separation, $x = 2852.6$ mm, $\alpha = 5°$.

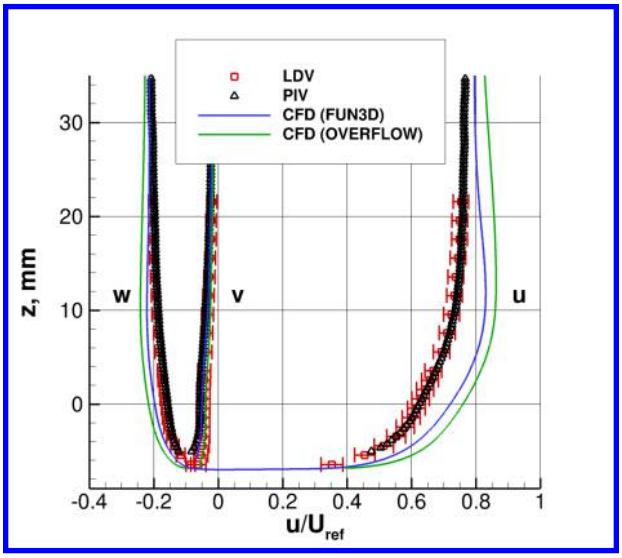

(a) Velocity profiles

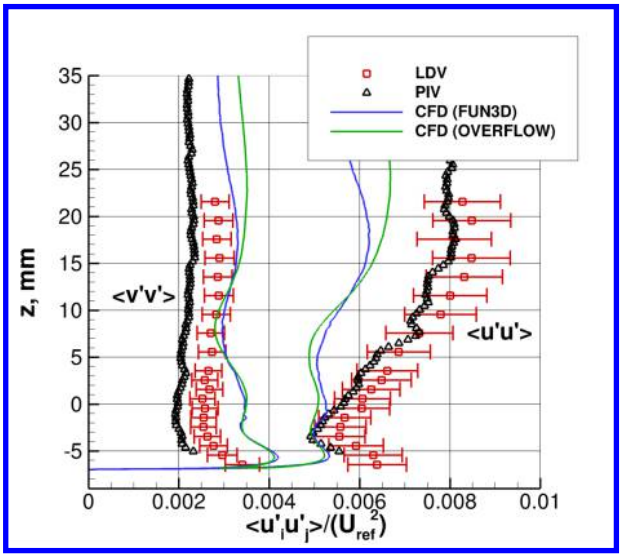

(b) Turbulence profiles (part 1)

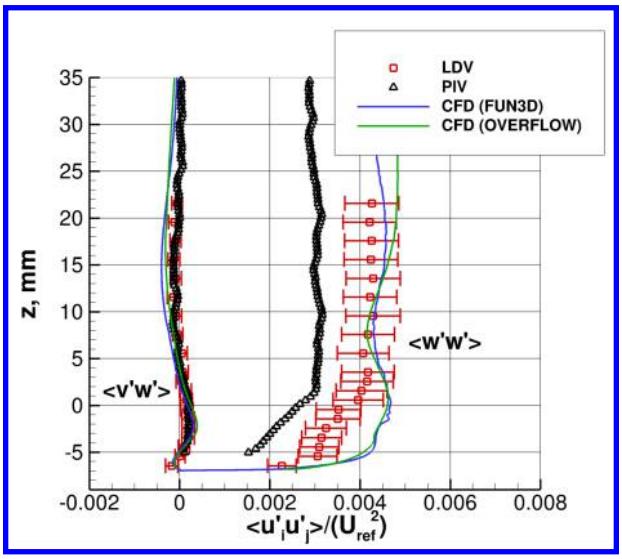

(c) Turbulence profiles (part 2)

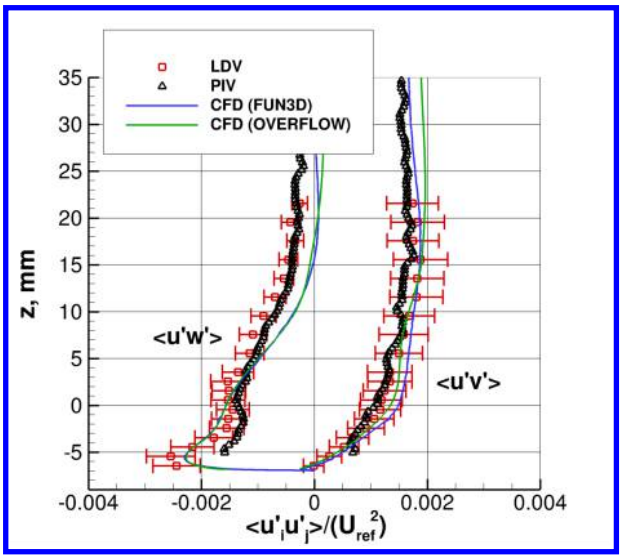

(d) Turbulence profiles (part 3)

Figure 25. Profiles along $x = 2852.6$ mm and $y = -246.1$ mm, $\alpha = 5°$.

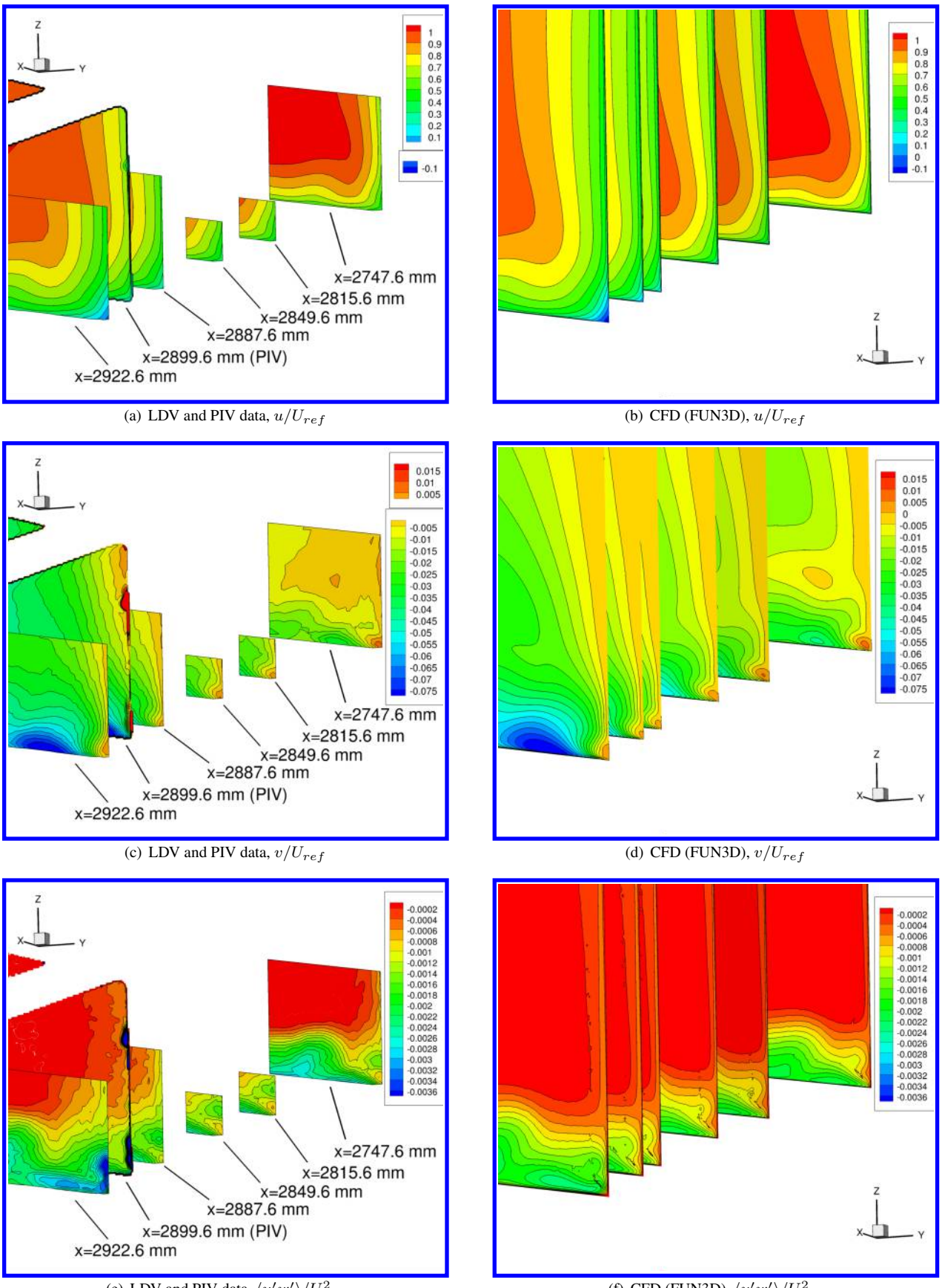

(a) LDV and PIV data, u/U_{ref}

(b) CFD (FUN3D), u/U_{ref}

(c) LDV and PIV data, v/U_{ref}

(d) CFD (FUN3D), v/U_{ref}

(e) LDV and PIV data, $\langle u'w' \rangle / U_{ref}^2$

(f) CFD (FUN3D), $\langle u'w' \rangle / U_{ref}^2$

Figure 26. Progression of selected contours of interest, $\alpha = -2.5^\circ$.